

manuscript submitted to *JGR: Solid Earth*

1 **Strong upper-plate heterogeneity at the Hikurangi
2 subduction margin (North Island, New Zealand)
3 imaged by adjoint tomography**

4 **Bryant Chow^{1,2}, Yoshihiro Kaneko³, Carl Tape⁴, Ryan Modrak⁵, Nick
5 Mortimer², Stephen Bannister², John Townend¹**

6 ¹School of Geography, Environment and Earth Sciences, Victoria University of Wellington

7 ²GNS Science

8 ³Department of Geophysics, Kyoto University

9 ⁴Geophysical Institute, University of Alaska Fairbanks

10 ⁵Los Alamos National Laboratory

11 **Key Points:**

- 12 • We develop a high-resolution (4–30 s) 3D velocity model of the North Island of
13 New Zealand with 28 adjoint tomography iterations.
14 • Distinct P- and S-wave velocity changes of up to $\pm 30\%$ are made to the existing
15 model in the upper 30 km.
16 • The tomographic results provide improved images of tectonic and magmatic struc-
17 tures throughout the Hikurangi subduction margin.

Corresponding author: Bryant Chow, bryant.chow@vuw.ac.nz

Abstract

We use adjoint tomography to invert for three-dimensional structure of the North Island, New Zealand and the adjacent Hikurangi subduction zone. Due to a shallow depth to the plate interface below the North Island, this study area offers a rare opportunity for imaging material properties at an active subduction zone using land-based measurements. Starting from a ray tomography initial model, we perform iterative model updates using spectral element and adjoint simulations to fit waveforms with periods ranging from 4–30 s. In total we perform 28 L-BFGS updates, improving data fit and introducing V_p and V_s changes of up to $\pm 30\%$. Resolution analysis using point spread functions show that our measurements are most sensitive to heterogeneities in the upper 30 km. The most striking velocity changes coincide with areas related to the active Hikurangi subduction zone. Lateral velocity structures in the upper 5 km correlate well with New Zealand geology. The inversion recovers increased along-strike heterogeneity on the Hikurangi subduction margin with respect to the initial model. In Cook Strait we observe a low-velocity zone interpreted as deep sedimentary basins. In the central North Island, low-velocity anomalies are linked to surface geology, and we relate velocity structures at depth to crustal magmatic activity below the Taupō Volcanic Zone. Our velocity model provides more accurate synthetic seismograms, constrains complex velocity structures, and has implications for seismic hazard, slow slip modeling, and understanding of volcanic and tectonic structures related to the active Hikurangi subduction zone.

Plain Language Summary

We perform seismic imaging of the Earth's crust below the North Island of New Zealand, which sits above an active plate boundary known as the Hikurangi subduction zone. By comparing computer simulations of earthquake ground motion to observed ground motion, our imaging method iteratively improves models of Earth structure. Our dataset consists of earthquake waveforms from 1800 unique source–receiver pairs. The chosen waveform frequencies relate to spatial resolution on the order of 5–50 km. We incrementally update the seismic velocities of the initial model 28 times resulting in velocity changes of up to $\pm 30\%$. Velocity heterogeneities are most strongly resolved in the upper 30 km. Seismic velocity structures in the upper 5 km correspond well with known surface geology. The strongest velocity changes correspond to regions related to the Hikurangi subduction zone, such as a deep sedimentary basin in Cook Strait, and anomalous velocity structures related to the Taupō Volcanic Zone. The newly derived velocity model improves predictions of earthquake ground motion, and has implications for seismic hazard, slow slip modeling, and understanding of volcanic and tectonic structures associated with the active Hikurangi subduction zone.

1 Introduction

In New Zealand, ray-based seismic tomography has produced detailed images of an active convergent plate boundary (Eberhart-Phillips et al., 2005; Eberhart-Phillips & Reyners, 2012; Eberhart-Phillips & Bannister, 2015; Eberhart-Phillips, Bannister, Reyners, & Henrys, 2020). These tomographic images have been used for earthquake relocation studies (e.g. Bannister et al., 2011; Reyners et al., 2011; Lanza et al., 2019), ground motion simulations (e.g. Bradley et al., 2017; Kaneko et al., 2019; Chow et al., 2020), and characterization of structures, material properties, and slip behavior related to the Hikurangi subduction zone (e.g., Williams et al., 2013; Reyners et al., 2017; Ellis et al., 2017; Williams & Wallace, 2018; Henrys et al., 2020). These images have also improved knowledge related to the potential for large, megathrust earthquakes that pose significant risk to New Zealand and the surrounding regions (e.g., Eberhart-Phillips et al., 2005; Cochran et al., 2006; Henrys et al., 2006; Reyners et al., 2006; Wallace & Beavan, 2006; Litchfield et al., 2007; D. Barker et al., 2009; Wallace et al., 2009; Fagereng & Ellis, 2009;

68 Wallace et al., 2014; Kaneko et al., 2018). Despite their wide utility, these models are
 69 derived using simplifying ray theory, which has been shown to lead to ambiguous inter-
 70 pretations of tectonic features (Marquering et al., 1999; Zhao et al., 2000; Dahlen et al.,
 71 2000; Hung et al., 2001; Dahlen & Baig, 2002). Modern advances in computational power,
 72 and progress in the field of seismic tomography, have ushered in an era of imaging us-
 73 ing full-waveform techniques. These techniques measure all or part of the time-dependent
 74 seismic waveform, rather than point measurements like traveltimes differences. Taking
 75 advantage of full-waveform tomography, this study seeks to improve a ray-based veloc-
 76 ity model of the North Island of New Zealand.

77 Adjoint tomography is a type of full-waveform inversion which 1) simulates seis-
 78 mic waves by solving the seismic wave equation (Tromp et al., 2005; Fichtner et al., 2006a,
 79 2006b; Tape et al., 2007), 2) iteratively improves numerical models using the adjoint-
 80 state method (Tarantola, 1984), and 3) in seismology, has historically focused efforts on
 81 inverting for short-period ($T > 2$ s) earthquake-generated surface waves (e.g., Tape et
 82 al., 2010; Fichtner et al., 2010; Krischer et al., 2015; Zhu et al., 2015; Tao et al., 2018).
 83 By solving the seismic wave equation, adjoint tomography honors the intrinsic physics
 84 of wave propagation, overcoming limitations inherent in ray theory (e.g., Montelli et al.,
 85 2004). The transition to full-waveform techniques has been accelerated by the develop-
 86 ment of efficient numerical solvers that accurately simulate seismic wave propagation at
 87 a wide range of scales (e.g., Komatitsch et al., 2002), and automated workflow tools which
 88 reduce the algorithmic complexity involved in large-scale inversions (e.g., Krischer et al.,
 89 2015; Modrak et al., 2018; Chow et al., 2020; Thrastarson et al., 2021). Despite its in-
 90 creased accuracy, typical resolutions in earthquake-based adjoint tomography are lim-
 91 ited to long-wavelength crustal and mantle structure (e.g., Fichtner et al., 2010; Zhu et
 92 al., 2015; Chen et al., 2015; Bozdağ et al., 2016; Tao et al., 2018; Krischer et al., 2018),
 93 or crustal structure in regional settings with sufficient seismicity and station coverage
 94 (Tape et al., 2010; Miyoshi et al., 2017).

95 New Zealand is characterized by high levels of seismicity, a permanent seismic net-
 96 work, and an existing regional 3D tomography model. In Chow et al. (2020) we demon-
 97 strated the feasibility of applying full-waveform tomography to the North Island of New
 98 Zealand through data-synthetic misfit assessment and realistic synthetic inversions. Build-
 99 ing upon this work, we undertake the first application of adjoint tomography in New Zealand
 100 to generate and interpret a high-resolution velocity model of the Hikurangi subduc-
 101 tion zone and the North Island of New Zealand. The main goals of this study are to:

- 102 1. Perform adjoint tomography for the North Island;
- 103 2. Assess the updated velocity model based on waveform improvement, velocity changes,
 and point spread functions;
- 104 3. Identify and interpret the most striking velocity changes.

105 The paper begins with an overview of the tectonic setting (Section 2). An explanation
 106 of methodologies (Section 3) is followed by a description of data used in the inversion
 107 (Section 4). Section 5 presents the final velocity model alongside an accompanying res-
 108 olution analysis (Section 6). The paper closes with a discussion of the most striking ve-
 109 locity changes (Section 7). A companion paper (Chow et al., companion manuscript) pro-
 110 vides a more detailed look at three specific velocity changes in the Hikurangi subduc-
 111 tion wedge, and their interpretations. In this paper we focus on interpretations of ve-
 112 locity changes in North Island basement terranes, Taupō Volcanic Zone, and Cook Strait.
 113

114 2 Tectonic setting

115 The Hikurangi subduction zone is a convergent plate boundary where the Pacific
 116 plate subducts westward beneath the Australian plate at a rate of ~ 40 mm/yr (Lewis
 117 & Pettinga, 1993; DeMets et al., 1994; Collot et al., 1996; Nicol et al., 2007; Barnes et

al., 2010). The margin exhibits substantial along-strike differences in structure and interseismic coupling (Wallace et al., 2004, 2009; Barnes et al., 2010). Much of the Hikurangi forearc above the shallow part of the plate interface is exposed sub-aerially due to buoyancy of the subducting plate (Litchfield et al., 2007; Nicol et al., 2007). The Hikurangi trench is consequently closer to the coastline—between 40 and 120 km (Figure 1)—in comparison with most well-studied subduction settings. The plate interface below land is located at ~15 km depth below the east coast of the North Island (Figure 2; Williams et al., 2013). In the area of Figure 1, the subducting Pacific plate mostly comprises the Hikurangi Plateau, a Cretaceous large igneous province (Mortimer & Parkinson, 1996; Taylor, 2006) that is considerably thicker than the subducting oceanic crust further north (Davy et al., 2008; Mochizuki et al., 2019). In the southern part of Figure 1, the Pacific plate consists of the thick (~23–26 km) continental crust of the Chatham Rise (Eberhart-Phillips & Reyners, 1997; Reyners et al., 2017).

New Zealand is commonly separated into lithologically distinct basement terranes, separated by faults or melanges, and overprinted by more recent tectonic processes (Mortimer, 2004; Edbrooke et al., 2015). In the North Island, a system of left-lateral strike-slip faults runs along the eastern edge of the island, and accommodates ~6 mm/yr of the total convergence in the north, to ~20 mm/yr in the south (Nicol & Beavan, 2003). In the central North Island, the active magmatic arc is represented by the calderas and volcanoes of the Taupō Volcanic Zone (TVZ). The TVZ is also a zone of active extension which is characterized by high heat flow and geothermal activity, extensional faulting, and corresponding seismicity (Wilson et al., 1995, 2009). The maximum rate of extension in the TVZ is 20 mm/yr (Villamor & Berryman, 2006). Further west, volcanism occurs at Mt. Taranaki, which is unusual in both its location and eruptive composition (Sherburn & White, 2006; Sherburn et al., 2006). Offshore of the west coast of the North Island are two large sedimentary basins, the Taranaki basin (e.g., King & Thrasher, 1996) and Whanganui basin (Carter & Naish, 1998). The Hikurangi subduction margin terminates below the northern South Island, where plate convergence becomes dominantly strike-slip along the Alpine fault (e.g., Sutherland et al., 2007; Wallace et al., 2007), after a complex transition from oblique subduction to oblique transpression in Cook Strait and through the Marlborough fault system (e.g., Pondard & Barnes, 2010; Eberhart-Phillips & Bannister, 2010; Reyners et al., 2017).

Seismic activity associated with the Hikurangi subduction zone is frequent and varied in terms of faulting mechanism and location (Ristau, 2008; Townend et al., 2012). Subduction seismicity is characterized by intraplate events within the subducting Pacific plate and interplate seismicity along the megathrust subduction interface. In the upper plate, seismicity is observed as extensional faulting of the central North Island (Darby et al., 2000; Villamor et al., 2017), and left-lateral strike-slip faulting along the length of the margin (Nicol & Beavan, 2003). In the northern South Island, the 2016 M_w 7.8 Kaikōura earthquake produced one of the most complex multi-fault rupture patterns observed (Hamling et al., 2017; Holden et al., 2017), with an extensive aftershock sequence (Lanza et al., 2019; Chamberlain et al., 2021). To the north, the 1947 M_w 7.0 Gisborne earthquake generated one of the largest tsunamis in New Zealand history (Bell et al., 2014).

Geodetic observations have been used to observe slow slip events (SSEs) and determine slip rate deficit along the Hikurangi plate interface (Wallace, Beavan, et al., 2012; Wallace, 2020). At the northern margin, SSEs have been observed offshore and close to the trench, where the plate interface is shallow at depths of 5–15 km (Wallace, 2020). In contrast, at the southern Hikurangi margin the plate interface is inferred to be locked to roughly 30 km depth, with SSEs observed at depths of 30–45 km (Wallace, Beavan, et al., 2012; Wallace, 2020). Wallace et al. (2009) proposed that if the geodetically locked southern portion of the Hikurangi margin were to slip seismically, it would be capable of producing a megathrust event as large as M_w ~8.2–8.7.

170

3 Methods

171 Adjoint tomography seeks to minimize data-synthetic misfit through iterative im-
 172 provements of model parameters that approximate sources and structure. In this study
 173 we undertake adjoint tomography following the methodologies outlined in Chow et al.
 174 (2020).

175

3.1 Forward modeling and misfit function

176 The forward problem solves the seismic wave equation given representations of an
 177 earthquake and Earth structure. For forward simulations we use the time-domain spec-
 178 tral element solver, SPECFEM3D Cartesian (Komatitsch & Tromp, 2002b, 2002a). To
 179 mesh the North Island, we use hexahedral elements and a rectangular domain with roughly
 180 450 km by 600 km horizontal extent and 400 km vertical extent. Topography and bathymetry
 181 are explicitly honored at 1 km spacing interpolated from SRTM-30P elevations (Becker
 182 et al., 2009). Elevations at the top of the mesh range ± 3 km, and no water layer is in-
 183 cluded. Because the minimum required element size decreases with depth, we include
 184 two coarsening layers in the mesh. At each coarsening layer, the horizontal element spac-
 185 ing doubles and vertical element spacing triples.

186 To avoid unnecessary computational expense in the early iterations, two mesh res-
 187 olutions are used over the course of the inversion. A coarse mesh with minimum element
 188 spacing of 2 km that is accurate down to 8 s period is used for the initial long-period it-
 189 erations. When the minimum waveform period falls below 8 s, a fine resolution mesh with
 190 minimum element spacing of 1 km is substituted. The fine-resolution mesh is accurate
 191 to 2.5 s period. The coarse- and fine-resolution meshes contain 88 000 and 220 000 el-
 192 ements, respectively.

193 The misfit between observed (data) and simulated (synthetic) seismograms is quan-
 194 tified using a windowed cross-correlation traveltime misfit function. All simulations are
 195 run for 300 s, starting 20 s prior to the earthquake origin time. To selectively restrict
 196 data included in the inversion, an automatic time-windowing algorithm is applied (Maggi
 197 et al., 2009), which ignores undesirable signals such as low signal-to-noise ratio obser-
 198 vations. Within a given time window i , the misfit function is defined as

$$\chi_i(\mathbf{m}) = \frac{1}{2} \left[\frac{T_i^{obs} - T_i(\mathbf{m})}{\sigma_i} \right]^2, \quad (1)$$

199 where T^{obs} is the observed traveltime, $T(\mathbf{m})$ is the corresponding synthetic traveltime
 200 for a model \mathbf{m} , and σ is a measurement uncertainty weight (Tromp et al., 2005). For each
 201 iteration, misfit defined by Equation 1 is averaged over all windows for a given event,
 202 and for all events in a given iteration. The objective function for a given model \mathbf{m} is de-
 203 fined as

$$F(\mathbf{m}) = \frac{1}{2S} \sum_{s=1}^S \frac{1}{N_s} \sum_{i=1}^{N_s} \chi_i(\mathbf{m}), \quad (2)$$

204 where S is the total number of sources, and N_s is the total number of windows for a given
 205 source s (Tape et al., 2010). Equation 2 is used as a measure for overall data-synthetic
 206 misfit for a given velocity model.

207

3.2 Inverse problem

208 The inverse problem seeks to iteratively improve the Earth model by minimizing
 209 the misfit function $F(\mathbf{m})$ (Equation 2). For each iterative model update, we first com-
 210 pute the gradient of the misfit function using the adjoint-state method (Tarantola, 1984;
 211 Tromp et al., 2005; Fichtner et al., 2006a; Tape et al., 2007). We then apply the L-BFGS
 212 inverse Hessian to the gradient to obtain a search direction (Nocedal & Wright, 2006).

Finally we calculate a step length along the search direction using a backtracking line search (Modrak & Tromp, 2016; Chow et al., 2020).

At each iteration, derivatives with respect to V_p and V_s are computed using the adjoint-state method, and V_p and V_s are updated. Density is held constant due to its limited sensitivity to the surface wave measurements primarily used (Nazarian & Stokoe, 1984). Attenuation is also held constant as the misfit function is only dependent on phase and not amplitude (Equation 1). Following Chow et al. (2020), we carefully select events from a reviewed catalog, and we do not perform source inversions to update hypocenters or moment tensors.

Regularization is often used in tomographic inversions to suppress nonuniqueness (Modrak & Tromp, 2016). In this work we smooth the gradient by convolution with a 3D Gaussian to suppress poorly-constrained high-wavenumber components of the updated models. Horizontal and vertical half-widths are chosen larger than the expected spatial resolution of input data to promote resolution of large-scale features in early iterations. Waveform bandpass and gradient smoothing length are reduced gradually throughout the inversion to conservatively approach the global minimum of the objective function (Figure 3).

4 Data

4.1 Study area and starting model

With the North Island of New Zealand as our study area, domain edges are chosen based on source and receiver locations as well as computational expense (Figure 2). Limited station coverage and a lack of large magnitude ($M_w > 4$), shallow (depth > 60 km) events ruled out including regions north of Auckland (37°S). The eastern boundary (178.5°E) is limited to the sub-aerial extent of the North Island, chosen to minimize the amount of deep-ocean model space with little data coverage. The southern (42.5°S) and western (173°E) boundaries are chosen to include a number of aftershocks and related seismicity from the 2016 $M_w 7.8$ Kaikōura earthquake (Hamling et al., 2017; Holden et al., 2017). In this work all locations are converted to, and shown in, the UTM 60S coordinate system.

The starting velocity model is defined by the NZ-Wide2.2 velocity model of Eberhart-Phillips, Bannister, Reyners, and Henrys (2020). This velocity model was developed using ray-based traveltimes tomography, and improved in areas with joint inversions of Rayleigh-wave group velocity maps (Eberhart-Phillips & Fry, 2017), and joint inversions with teleseismic surface waves (Eberhart-Phillips & Fry, 2018). This 3D velocity model defines V_p , V_p/V_s , density and attenuation (Q_p , Q_s ; Eberhart-Phillips et al., 2015, 2017; Eberhart-Phillips, Bannister, & Reyners, 2020) for the entire New Zealand region. In this work we derive a corresponding V_s model using the NZ-Wide2.2 V_p and V_p/V_s models. In Chow et al. (2020) we assessed waveform misfits for 250 regional earthquakes using this starting velocity model and showed that data-synthetic time shifts for >25 000 measurements are reasonable for adjoint tomography.

4.2 Earthquake sources

We select 60 earthquakes with high signal-to-noise ratio waveforms recorded between 2004 and 2019 (Figure 2; Table S1). In the target bandpass of 4–30 s, surface waves are the dominant signals. Event magnitudes range $4.5 \leq M_w < 6.0$ with depths less than 60 km. In general, waveforms from events with $M_w < 4.5$ are recorded by only several stations in the network, limiting their usefulness at the regional scale. Events with $M_w \geq 6.0$ are also excluded because our simulations use point source approximations, while large magnitude events may require finite fault solutions for accurate synthetic wave-

261 forms. Moment tensors in New Zealand are routinely calculated by GeoNet (Ristau, 2008)
 262 using the Time Domain Moment Tensor algorithm (Dreger, 2003), and are available for
 263 regional earthquakes since 2003.

264 Although the initial catalog of suitable events contains \sim 250 events, a large number
 265 of these are foreshock and aftershock sequences, which densely cluster certain regions
 266 of the domain with spatially and mechanically similar earthquakes. These events pro-
 267 duce near-identical waveforms at the period range of interest (4–30 s), and without any
 268 explicit weighting considerations (e.g., Ruan et al., 2019), repeated contributions from
 269 such source–receiver paths are observed to have an undesired effect on the inversion. Stacked
 270 contributions from these paths mask out more unique source–receiver paths during the
 271 inversion, leading to anomalously strong contributions in regions with dense event clus-
 272 tering.

273 To downweight the contributions of clustered events, we perform event declustering
 274 during which we grid the model domain into 10×10 horizontal bins, and 2 vertical
 275 sheets (depths of 0–20 km and 20–200 km), totalling 200 grid cells. We specify that
 276 only two events from the initial catalog can be retained per grid cell, leading to more uni-
 277 form coverage throughout the domain and a preferential selection of crustal (< 20 km)
 278 events. Events recorded on temporary stations are also prioritized to ensure unique re-
 279 ceiver locations are included. We choose a final catalog size of 60 events to maximize the
 280 number of unique event locations without including too many similar locations or mo-
 281 ment tensors (Figure 2). From the remaining catalog we select 60 additional events with
 282 the same magnitude and depth range as a validation catalog for later model assessment
 283 (Section 5.4).

284 4.3 Receivers

285 Broadband seismic data is collected for 88 three-component broadband stations from
 286 permanent and temporary networks (Figure 2; Table S1). The permanent seismic net-
 287 work of New Zealand is operated by GeoNet (<https://www.geonet.org.nz/>), with 38 broad-
 288 band stations located within the study area. Data from an additional 50 broadband sta-
 289 tions are included. In total, 1800 unique source–receiver paths are used (Figure 2), with
 290 temporary network data providing roughly 8% of the initial dataset.

291 Temporary seismometer deployments throughout the North Island are used to en-
 292 hance coverage of the permanent network. For this adjoint tomography study, the Broad-
 293 band EAst COast Network (BEACON) was deployed in southern Hawke's Bay (Kaneko
 294 & Chow, 2017). BEACON consisted of 22 broadband, three-component station locations
 295 which recorded for 1.5 years between 2017 and 2019 (Text S1). In the southern North
 296 Island, the Seismic Analysis of the HiKurangi Experiment (SAHKE) transect consisted
 297 of a line of broadband and short-period seismic receivers deployed perpendicular to the
 298 trench to capture offshore shots and image plate interface characteristics (Henrys et al.,
 299 2013). Our dataset includes broadband data from the SAHKE line, as well as two de-
 300 ployments focused on the Taupō Volcanic Zone (Bannister, 2009) and the Gisborne re-
 301 gion (Figure 2; Table S2; Bannister & Bourguignon, 2011).

302 5 Results

303 We present the results of our inversion and the final velocity model (M28; Figure 4).
 304 Model differences with respect to the initial model (M00) are shown in terms of net model
 305 update $\ln(M_{28}/M_{00})$, which to first order approximates the percentage difference ($M_{28}/M_{00} - 1$)
 306 but more reliably represents model differences over a wide range of values with respect
 307 to the percentage difference (Tape et al., 2007).

308 Heterogeneous velocity changes are recovered best in V_s , so we primarily discuss
 309 V_s and V_p/V_s structures in the following sections. We also address waveform improve-
 310 ment for select source–receiver pairs (Figure 8) and in total (Figure 9).

311 5.1 Inversion legs

312 We perform 28 L-BFGS iterations over six distinct inversion legs (Figure 3). The
 313 start of each inversion leg is defined by selection of new time windows and a change of
 314 input parameters including some or all of: waveform bandpass, windowing algorithm pa-
 315 rameters, gradient smoothing length.

316 To help ensure convergence to the global minimum, we progress from low to high
 317 frequencies over the course of the inversion (e.g., Fichtner et al., 2009; Tape et al., 2010;
 318 Krischer et al., 2018). New time windows are chosen at the beginning of each leg, and
 319 remain mostly fixed throughout a given leg to ensure that misfit assessment compares
 320 a similar segment of the dataset. Time windowing parameters are modified slightly at
 321 each leg to reflect changes in input parameters.

322 The choice to begin a new inversion leg was in some cases motivated by the behav-
 323 ior of the nonlinear optimization algorithm. Loss of descent direction, negligible misfit
 324 reduction, or a large number of step counts in the line search (>5) can be indicators of
 325 convergence within a given passband. In such cases, we discard the accumulated L-BFGS
 326 history and move on to a new leg. However, because restarting the nonlinear optimiza-
 327 tion is computationally expensive, we discard L-BFGS history only when signs of numer-
 328 ical stagnation, like those above, are present. At the start of each leg, multiple trial it-
 329 erations are performed to determine a suitable set of windowing parameters, waveform
 330 bandpass, and smoothing length. Characteristics for an acceptable suite of parameters
 331 include similar misfit and number of measurements as the previous iteration.

332 Mesh resolution was changed between inversion legs D and E (Figure 3) to accom-
 333 modate higher frequency waveforms. This method saved roughly 400 000 CPU-hours by
 334 allowing the initial four inversion legs to be performed on a low-resolution mesh. How-
 335 ever, due to the dissimilar mesh constructions, the change required interpolation between
 336 regular and irregular grids. As a result, mesh artefacts are visible at depths correspond-
 337 ing to coarsening layers of the coarse mesh (e.g. Figure 4E). These artefacts are only vis-
 338 ible in regions with little to no resolution (e.g. southeast of the Hikurangi trench); they
 339 do not affect waveform propagation simulations and therefore do not impact our inter-
 340 pretations.

341 5.2 Velocity changes

342 The final velocity model shows large, heterogeneous velocity changes with respect
 343 to initial values within the 3D model (Figure 4). The maximum net model update val-
 344 ues are +0.33 for V_s (Figure 5) and +0.25 for V_p (Figure 6). The most striking hetero-
 345 geneities are visible at mid-crustal depths (15 km; Figure 4D–F) which taper off by 25 km
 346 (Figure 4G–J). In general, the final model is characterized by slower wavespeeds, with
 347 specific areas requiring substantial positive velocity changes. Most of the changes do not
 348 introduce new features, but rather serve to modify existing velocity features through changes
 349 in wavespeed, as well as sharpening and shifting of existing velocity gradients (Figure 4).

350 Moderate-sized (>50 km) shallow (<5 km) features like the low-velocity accretionary
 351 wedge, the high-velocity axial mountain ranges, and the low-velocity Taranaki and Whangamui
 352 basins (Figure 1), are identifiable in both initial and final models (Figure 4A, B). These
 353 similarities are expected since the longest waveform period of 30 s corresponds to spa-
 354 tial resolutions less than 100 km, for an average V_s of 3 km/s. On average, velocity changes
 355 range in values from ±5–20% in upper top 30 km, with velocity changes above ±1% at
 356 depths less than 75 km. By 100 km depth the two models are the same due to the lim-

357 ited depth sensitivity of 30 s surface waves. At 25 km depth (Figure 4I), large (>50 km)
 358 features are characterized by the plate interface region, with the high-velocity Pacific plate
 359 contrasting the slower relative velocities of the upper Australian plate. As expected, in
 360 regions with sparse data coverage (i.e. deep ocean, offshore the west coast of the North
 361 Island), recovered velocity changes are negligible.

362 Consecutive net model updates at 5 km depth (Figures 5, 6) show the final iteration
 363 of each inversion leg (Figure 3), which provides a qualitative look at model changes
 364 in V_s (Figure 5) and V_p (Figure 6). In V_s , initial resolution of long-wavelength (>100 km)
 365 structure (Figure 5A) is gradually improved with increasing detail (Figure 5B–F). The
 366 most striking velocity features (labels A–E), are already visible by the second inversion
 367 leg (Figure 5B), suggesting that they were necessary to fit the initial long-wavelength
 368 data-synthetic misfit. The last two inversion legs (Figure 5E, F) mainly serve to sharpen
 369 existing features and increase detail. Consecutive V_p updates follow a similar trend as
 370 V_s (Figure 6), although the amplitude of change is less severe, likely because the initial
 371 ray-based model was derived primarily using P-wave direct arrivals.

372 Crustal heterogeneity at 5 km depth is visually dominated by three, strong, (> 20%)
 373 positive velocity changes, labelled A, B, and C in Figure 4. These perturbations intro-
 374 duce positive velocity anomalies in the forearc region, visible directly beneath A) Māhia
 375 Peninsula, B) Pōrangahau, and C) the northern South Island. Adjacent to the positive
 376 velocity anomaly Feature C is a low-velocity perturbation offshore (e.g., Figure 4B, C).
 377 Together these velocity changes image a strong velocity gradient in the transition from
 378 the South Island to Cook Strait. In the central North Island, at 5 km depth, slow ve-
 379 locities in the TVZ (feature D) are bounded by high velocities to the east and west (Fig-
 380 ure 4B). This strong gradient is most prominent at 5 km depth (Figure 4B) and is no
 381 longer visible by 25 km depth (Figure 4H). Offshore Pōrangahau, feature E highlights
 382 a localized, negative velocity change which is most visible as a strong low-velocity anomaly
 383 at 25 km depth (Figure 4H, I).

384 The ratio of seismic velocities (V_p/V_s) is often used in tomographic studies in con-
 385 junction with interpretations of absolute velocity; high V_p/V_s has been inferred to cor-
 386 relate with increased clay content in sedimentary rocks, increased porosity, highly frac-
 387 tured rocks, and increased fluid pressures (e.g., Christensen, 1996; Ito et al., 1979; Eberhart-
 388 Phillips et al., 1989, 2005; Audet et al., 2009). With increased sensitivity to V_s struc-
 389 ture through the predominance of surface waves measurements, we see strong changes
 390 in the M28 V_p/V_s model, shown at 5 km depth in Figure 7. We note that the net model
 391 updates of V_s (Figure 4C) and V_p/V_s ratio (Figure 7C) show strong similarities, hint-
 392 ing that the resolved differences in V_p/V_s are predominately related to changes in V_s
 393 structure. This makes sense as we expect the strongest velocity changes in V_s where the
 394 initial velocity model would have lacked resolution. Similarly, heterogeneous V_p updates
 395 indicate that changes in V_p also contribute to updates in V_p/V_s (Figure 6).

396 5.3 Waveform improvement

397 Waveforms show considerable improvement from the initial (M00) to final (M28)
 398 velocity models, but data-synthetic misfits still remain by M28 (Figure 8). Here we dis-
 399 cuss waveforms at 6–30 s to emphasize longer-period surface wave signals, because wave-
 400 forms at 4–30 s begin to show lower signal-to-noise ratios and are therefore less illustra-
 401 tive of waveform improvement.

402 Data-synthetic misfit is compared in Figure 8 for eight representative source-receiver
 403 pairs. Direct (P) arrivals are well fit by the initial model, which is to be expected from
 404 a tomography model derived from body-wave traveltimes (e.g. Figure 8A). Surface waves
 405 and later arrivals in the initial model show considerable time shift with respect to the
 406 data at this bandpass (e.g. Figure 8B, C). Paths which pass through relatively simple
 407 crustal structure (e.g. Figure 8E–H) show better initial waveform fit with respect to ray-

408 paths that travel near or through more complex tectonic regions such as the low-velocity
 409 accretionary wedge (e.g. Figure 8B–D). The large initial misfit of an offshore source (Figure
 410 8D) shows the limited accuracy of the initial model away from land.

411 After the inversion, long-period (>10 s) time shifts are reduced to <1 s and sur-
 412 face waves for all waveform shown are mostly fit, although high-frequency components
 413 show varying degrees of misfit (Figure 8E). Some synthetics—both in M00 and M28—
 414 show high-frequency components not seen in data (Figure 8C). Amplitude information,
 415 which is not inverted for, shows little to no improvement, and in most cases data-synthetic
 416 amplitude differences do not change (Figure 8C). Errors in high frequencies and ampli-
 417 tudes might be attributable to inaccuracies in the underlying attenuation model at short
 418 periods, since it is not updated during the inversion. Similarly, coda waves are left mostly
 419 unimproved (e.g. Figure 8D), hinting at the difficulty of accurately resolving small-scale
 420 heterogeneities and basin effects caused by sharp impedance contrasts (e.g., Kaneko et
 421 al., 2019).

422 5.4 Bulk misfit assessment

423 Total normalized misfit (Equation 2) is reduced over the 28 iterations (Figure 3).
 424 The largest ($>10\%$) relative reductions in misfit occur in the initial long-period inver-
 425 sion legs, A and B (Figure 3). Total seismogram window length is also maximum here
 426 at 500 000 s or 138 h. At Leg C, an attempt to reduce gradient smoothing while retain-
 427 ing bandpass was made. The negligible misfit reduction suggests that the previous in-
 428 version leg B was capable of fitting the 10–30 s period range (Figure 3). At 8–30 s (Leg
 429 D) another large decrease in overall misfit occurs. By 6–30 s (Leg E) the behavior of the
 430 misfit reduction is less pronounced than earlier inversion legs (Figure 3).

431 For later inversion legs (E, F), signal-to-noise ratio increased as the waveform band-
 432 pass included more high-frequency noise signals such as the secondary microseism (5–
 433 10 s; Webb, 1998). This is noted in the large decrease in total measurements for the 4–
 434 30 s period band (Figure 3). Total measurement length here is roughly 60 h, less than
 435 half of the initial inversion legs. After the final model, a number of trial iterations were
 436 run on an ultra-fine resolution mesh using 3–30 s waveforms. At these shorter periods,
 437 observed waveform signal-to-noise ratio increased further and misfit reduction was neg-
 438 ligible with respect to previous inversion legs. At this point, we decided to terminate the
 439 inversion.

440 Histograms are a useful method for showing time shifts and amplitude differences
 441 in bulk (Figure 9). Amplitude differences here are defined as $\Delta \ln A = \ln[\int d^2(t)dt / \int s^2(t)dt]$,
 442 where d and s are observed and synthetic waveforms, respectively (Dahlen et al., 2000).
 443 Bulk misfit assessment for 6–30 s is performed for the initial and final models using the
 444 60 inversion events (Figure 9A, B) and 60 separate post-hoc events (Figure 9C, D). The
 445 inversion time shift histogram shows that the initial time shift of 2.0 ± 3.9 s is reduced
 446 to 0.5 ± 3.7 s by the final model (Figure 9A). Amplitude differences show negligible change
 447 between initial and final models, which is expected since we use a phase-only misfit func-
 448 tion (Figure 9B, D). The post-hoc histograms show similar behavior to the inversion re-
 449 sults (Figure 9C, D), suggesting that the overall velocity changes have resolved mean-
 450 ingful structure, evidenced by improvement of data not included in the the inversion.

451 5.5 Computational expense

452 The total inversion required approximately 500 000 CPU-hours on the New Zealand
 453 eScience Infrastructure’s high performance computer, named Māui. Forward simulations
 454 require 0.5 h on 40 cores for the coarse-resolution mesh, and 0.75 h on 80 cores for the
 455 fine-resolution mesh. For each iteration, 60 forward simulations and 60 adjoint simula-
 456 tions are performed to generate synthetics and gradient, respectively. Gradient smooth-

457 ing occurs once per iteration at the cost of approximately one forward simulation. Wave-
 458 form preprocessing and misfit quantification are run in serial, and totalled roughly 2000 CPU-
 459 hours for the entire inversion.

460 An additional $60 \times N$ forward simulations are required for the line search to find
 461 an acceptable step length that suitably reduces the objective function. If the L-BFGS
 462 search directions are well scaled, then only one line search step should be required (Modrak
 463 & Tromp, 2016). In practice, N ranged between 1 and 3 for each iteration. If N reached
 464 values greater than 5, a new inversion leg was started.

465 6 Resolution analysis

466 Resolution information is important for assessing tomographic inversions, partic-
 467 ularly when the velocity models are used for interpretations of Earth structure and tec-
 468 tonic processes. However, exhaustive tomographic model assessment techniques are com-
 469 putationally infeasible with large, heterogeneous velocity models (e.g., Tarantola, 2005;
 470 Nolet, 2008). One method for resolution testing in full waveform tomography is the point
 471 spread function (Fichtner & Trampert, 2011b), which has been used in previous adjoint
 472 tomography studies (e.g., Zhu et al., 2015; Bozdağ et al., 2016; Tao et al., 2018).

473 Point spread functions (PSF) are a measure of how much a point-localized pertur-
 474 bation is smeared, or blurred, by the inversion procedure. Fichtner and Trampert (2011b)
 475 showed that the action of the Hessian on a model perturbation $\mathbf{H}(\mathbf{m})\delta\mathbf{m}$ can be viewed
 476 as a conservative estimate of the PSF, providing practical information on the extent to
 477 which features in a tomographic model can be interpreted. In practice we calculate PSFs
 478 using a finite-difference approximation

$$\mathbf{H}(\mathbf{m})\delta\mathbf{m} \approx \mathbf{g}(\mathbf{m} + \delta\mathbf{m}) - \mathbf{g}(\mathbf{m}), \quad (3)$$

479 where $\mathbf{H}(\mathbf{m})$ denotes the Hessian evaluated at the final model \mathbf{m} , $\mathbf{g}(\mathbf{m})$ the gradient eval-
 480 uated at the final model, and $\delta\mathbf{m}$ is a local model perturbation with respect to the fi-
 481 nal model.

482 We denote PSFs in the form H_{XY} , where X defines the quantity in which the per-
 483 turbation is made (V_p or V_s), and Y denotes the quantity defining the recovered point
 484 spread function. For example H_{SS} refers to a V_s point spread function for a perturba-
 485 tion in V_s , whereas H_{PS} quantifies parameter trade-offs, and shows the effect of a V_p
 486 perturbation on V_s recovery.

487 6.1 Individual point spread functions

488 To probe the resolution of individual features in our velocity model, we define a
 489 perturbation at a discrete point in the model and recover $\delta\mathbf{m}$ using Equation 3. The mo-
 490 tivation for each point-localized perturbation is to probe the robustness of features in
 491 terms of size, shape, and location. We define perturbations as 3D Gaussians with dif-
 492 ferent horizontal (σ_h) and vertical half-widths (σ_z). The full-width of the Gaussian is
 493 defined as $\Gamma = \sqrt{8}\sigma$. Since we are investigating V_s velocity anomalies, perturbation are
 494 made in V_s with peak amplitudes equal to $\pm 15\%$ of background M28 V_s model values.
 495 We place these perturbations at various locations around the model, corresponding to
 496 the prominent velocity features (A–E) discussed in Section 5. The results for features
 497 B and C are discussed in Section 7 alongside tectonic interpretations. The point spread
 498 functions for features A, B, and E are discussed in detail in Chow et al. (companion manuscript).

499 One example of a point spread test is shown in Figure 10. The positive-velocity per-
 500 turbation is defined at 12 km depth below the central North Island, with horizontal and
 501 vertical full-width of 10 km and 5 km, respectively (green circles; Figure 10A–B). The
 502 peak amplitude of the Gaussian is 15% of the final V_s velocity model or approximately

503 400 m/s. We apply this perturbation to the final M28 V_s model and calculate $\mathbf{g}(\mathbf{m} + \delta\mathbf{m})$ in the same manner as Section 3 to recover the PSF (Equation 3). As in the inversion, we apply regularization to this gradient to suppress unwanted high-wavenumber
504 components.
505
506

507 The resultant PSF (Figure 10C–D) shows acceptable recovery of the central peak
508 (dark colors; Figure 10C), but in cross-section the peak is smeared ~ 5 km above the in-
509 put location (Figure 10D), suggesting some uncertainty in recovering its exact depth. Out-
510 side of the full-width of the Gaussian, where perturbation amplitudes fall below 5% of
511 the final V_s velocity model, lateral smearing of about 1.5–2 times the size of the actual
512 perturbation (Figure 10A–B) is visible in both the horizontal and vertical directions (orange-
513 red colors; Figure 10C–D). This is likely due to regularization and limited resolution of
514 the dataset to such low-amplitude perturbations. The lowest-amplitude region of the PSF
515 (yellow colors; Figure 10C–D) shows patches to the north and south, suggesting that lim-
516 ited constraint of the dataset in these regions will result in minor velocity changes far
517 from the responsible anomaly.
518

518 6.2 Zeroth moment test

519 For insight into how resolution varies not just for individual features, but across
520 the entire model, we evaluate the action of the Hessian on a constant volumetric V_s per-
521 turbation $\delta\mathbf{m} = 50$ m/s using Equation 3. The result, shown in Figure 11, is equal to
522 the Fourier transform of the Hessian at zero wavenumber, or the zeroth moment (Fichtner
523 & Trampert, 2011a).

524 Similar to the ray-coverage plot in Figure 2B, the zeroth order moment test pro-
525 vides information about how resolution varies in a relative sense throughout the model,
526 but does not measure resolution length directly. In the case of uniform volumetric data
527 coverage, full recovery of the volumetric perturbation might be possible. In practice, how-
528 ever, significant departure from full recovery results from the limited sensitivity of the
529 dataset to structure outside the source–receiver configuration. Slices through the recov-
530 ered zeroth order moment are shown in Figure 11. A threshold value is chosen man-
531 ually to outline a volume in which velocity changes may be interpreted. The largest rel-
532 ative amplitudes of the zeroth moment are found in the top 10–15 km (Figure 11A, D,
533 E), reflecting the dominant influence of surface waves in our dataset. Interestingly, these
534 surface waves travelling through the low-velocity accretionary wedge and forearc basins
535 extend sensitivity of land-based measurements 50–100 km offshore (Figure 11A, B). With
536 increasing depth, the lateral extent of the zeroth moment shrinks. By 25 km depth, sen-
537 sitivity is primarily limited to below land (Figure 11C). Vertical cross sections reveal that
538 the dataset is sensitive to structure down to 50 km, however the strongest relative sen-
539 sitivity is limited to the top 20–30 km (Figure 11D, E). Based on the zeroth moment cov-
540 erage, we confine our interpretations to the upper 30 km.
541

541 7 Discussion

542 7.1 Comparisons with geology and tectonics

543 The structure of our updated velocity model has several points of comparison with
544 the known geologic basement terranes of New Zealand and their sedimentary and vol-
545 canic cover (Figure 12A; Mortimer, 2004; Edbrooke et al., 2015). In this section we make
546 comparisons between geology and our updated V_s model, but note that V_p and V_p/V_s
547 structures follow similar trends as V_s (Figure 12C, D).

548 Regional-scale (100s km) shallow velocity structures are broadly controlled by the
549 contrast between the exposed basement terranes to the west ($V_s > 2.5$ km/s), and the low-
550 velocity forearc basin and accretionary wedge to the east ($V_s < 2$ km/s; Figure 12A, B).

551 The boundary between these two tectonic features lies inland of the East Coast and spa-
 552 tially correlates with the axial ranges separating the volcanic arc and forearc basins, as
 553 well as the Esk Head Melange separating the Kaweka and Pahau/Waioeka terranes (black
 554 dashed line, Figure 12A). In V_p/V_s this boundary is less defined but spatially similar.
 555 The juxtaposition of high V_p/V_s (> 2) in the forearc region against low V_p/V_s (< 1.8)
 556 to the west may be the boundary between lower-velocity, fluid-saturated forearc sedi-
 557 ments and exposed basement rocks of the upper plate (Figure 12C). Visible in both V_s
 558 and V_p/V_s along this boundary are shallow, upper-plate expressions of the two high-velocity,
 559 low V_p/V_s anomalies identified as features A and B in Section 5. These are discussed
 560 in detail in Chow et al. (companion manuscript).

561 Moderate-sized features (~ 50 km) correspond well to basement terranes and in-
 562 dividual tectonic features around the North Island. High velocities ($V_s > 3$ km/s; Figure 12B)
 563 and moderate to low V_p/V_s (< 1.8 ; Figure 12C) below the central North Island strik-
 564 ing northeast–southwest show good agreement with the Waioeka, Kaweka, and Rakaia
 565 greywacke and schist terranes (Figure 12A). In the northeast near East Cape, a notch
 566 of high velocities ($V_s > 2.5$ km/s; Figure 12B) shows similar shape to the boundary be-
 567 tween the Pahau terrane and the East Coast Allochthon, a body of tectonically displaced
 568 sedimentary and volcanic rock. West of the TVZ, high velocities ($V_s > 3.5$ km/s) extend
 569 northward, spatially correlating with the western boundary of the Morrinsville terrane
 570 (Figure 12A). Corresponding high velocities are not seen in V_p (Figure 12D), potentially
 571 due to more limited V_p resolution in this region. In the northern South Island, the Caples
 572 terrane is overprinted by high-velocity schist, and has previously been associated with
 573 a distinct patch of high V_p (Eberhart-Phillips et al., 2005). V_s structures show a patch
 574 of high velocity ($V_s \approx 3$ km/s) extending offshore, generally coinciding with the offshore
 575 extent of the Caples terrane (Figure 12B)

576 Other geologic features can be related to non-basement geologic features of the the
 577 North and South Islands. In the TVZ, low velocity ($V_s < 2.5$ km/s) and high V_p/V_s ($>$
 578 1.8) extending from Ruapehu northwest into the Bay of Plenty (Figure 12B) is likely re-
 579 lated to magmatic processes in the active volcanic arc. Distinct low-velocity anomalies
 580 ($V_s \sim 2$ km/s), tens of km wide, make up the low-velocity zone seen in the TVZ, which
 581 are not visible in V_p (Figure 12D), resulting in resolution of high V_p/V_s (> 1.8) egg-
 582 shaped anomalies (Section 7.4; Figure 12C). Patches of low velocity crust are seen along
 583 the west coast of the North Island and are likely associated with the rubbly, low-porosity
 584 ring plain of Taranaki Volcano and with low-velocity sediments in the Taranaki and Whanganui
 585 Basins (Figure 12A). In the southern end of the study area, strong velocity gradients are
 586 imaged separating high velocity ($V_s > 3$ km/s) of the North and South Islands with low
 587 velocities ($V_s < 2$ km/s) in Cook Strait (Section 7.3).

588 Comparisons with two geologic cross sections along the East Coast show shallow
 589 (< 10 km) vertical resolutions at the scale of kilometers (Figure 13). In the two exam-
 590 ples crossing through northern Hawke's Bay (Figure 13C, E) and central Hawke's Bay
 591 (Figure 13D, F), the final V_s model shows low velocity layers agreeing with the geom-
 592 etry of the 20–30 km-scale faulted anticlines and synclines that extend from the surface
 593 down to ~ 10 km depth. These features are visible at both Northern and Central Hawke's
 594 Bay, providing a link between V_s structure and geologic observations of crustal struc-
 595 ture, deposition age, and sedimentary composition (Francis et al., 2004). Feature A (Fig-
 596 ure 4) is also visible at depth in northern Hawke's Bay (Figure 13E), and is discussed
 597 in further detail in Chow et al. (companion manuscript).

598 7.2 Along-strike crustal heterogeneity

599 Material heterogeneity along the strike of the Hikurangi has been proposed as an
 600 explanation for the observed locked-to-creeping transition zone of the plate interface (Reyners
 601 et al., 2017). In the NZ-Wide2.2 velocity model, Reyners et al. (2017) relate high V_p/V_s

(> 1.73) in the north with low slip rate deficit (blue interface line in Figure 14A). They explain the southward transition to low V_p/V_s values (< 1.73) as a progressive decrease in upper plate fluid content (red interface line in Figure 14A). In conjunction with re-located seismicity, Reyners et al. (2017) proposed that along-strike fluid distributions arise from variations in permeability of the overlying basement terranes, postulating that the Rakaia terrane (solid yellow lines in Figure 14A, B, D, E) acts as a permeability barrier, surrounded by a more permeable Pahau terrane (Figure 12A).

In contrast to the findings of Reyners et al. (2017), our final V_p/V_s model does not show the same southward linear transition from high to low V_p/V_s along strike, but rather strong heterogeneity and alternating patches of high and low V_p/V_s along strike (Figure 14B). If terrane boundaries are the cause of fluid distribution in the upper plate, then we would expect to see these patches correlate to terrane transitions. The yellow line on Figure 14B denotes the approximate location of the Rakaia terrane, surrounded by the Pahau terrane (Figure 12A), showing little correlation of V_p/V_s and terrane boundaries. Similarly strike-parallel cross sections through the Rakaia terrane show varying values of V_p/V_s (Figure 14D, E).

The final velocity model suggests that V_p/V_s structures are correlated more to the juxtaposition of a low-velocity (high- V_p/V_s) saturated forearc region, against low V_p/V_s basement terranes of the North and the South Islands (Figure 14B). One potential explanation for the discrepancy between initial and final V_p/V_s models may be our method's increased sensitivity to shallow V_s structure through the predominant use of surface wave measurements. We do observe that terrane boundaries exert control on upper plate heterogeneity through velocity structures (Section 7.1), however permeability control by upper plate composition seems to be insufficient to explain the heterogeneous V_p/V_s structures we observe.

7.3 Cook Strait velocity gradients

A strong velocity gradient in Cook Strait is imaged in the upper 10–15 km. It is defined by a low-velocity anomaly in Cook Strait, with steep, near-linear gradients near the coasts of the North and South Islands (labels N and S in Figure 15). On the basis of negative gravity anomalies and significant two way travel times (3–4 s TWT), Uruski (1992) identified three sedimentary basins in Cook Strait, suggesting >3 km deep sediment fills. Low-velocity sediments within these deep basin structures may be the source of the shallow, low velocities imaged in Cook Strait. In cross section, the gradients between these inferred basins and the North and South Islands are significant (Figure 15E, F). The northern boundary shows gradual relief with velocities reducing from approximately 3 km/s to 2 km/s across the transition (Figure 15C). The southern boundary separating Cook Strait and South Island shows a stronger contrast from 4 km/s to 2 km/s over 50 km distance (Figure 15E).

We use a PSF to probe resolution in this region (Figure 15C, G). The perturbation $\delta\mathbf{m}$ is a shallow (3 km depth), negative velocity perturbation, whose full-width is chosen to match the size of the low-velocity anomaly (Figure 15A). The amplitude of the resulting PSF is peaked offset from the perturbation and smeared in a roughly northeast–southwest direction (Figure 15B). In cross section the PSF suggests that a shallow velocity perturbation will be smeared a few km to depth. We interpret the results of the point spread function to suggest that the broad structure (50 km) of the low-velocity anomaly in Cook Strait is well-resolved, however the exact location and spatial extent of these features will be affected by smearing and lateral uncertainty.

These velocity gradients can be corroborated with additional evidence. Henrys et al. (2020) observe an abrupt crustal transition zone (hatched pattern in Figure 15A; black rectangles in Figure 15C, E), which coincides with our northern velocity gradient. This transition zone has previously been proposed as the ancient, rotated, Alpine-Wairau fault

(Little & Roberts, 1997; Barnes & Audru, 1999). A structural boundary here has also been proposed to be the faulted edge of North Island basement rocks (Holdgate & Grapes, 2015). Seismicity in the South Island appears to correlate with the southern velocity gradient (Figure 15A). The northern extent of large magnitude ($M>5$) earthquakes (GeoNet) and relocated Kaikōura aftershock seismicity (Figure 15B; Chamberlain et al., 2021) seem to coincide with the structural contrast here. This may be related to the sharp transition from exposed continental crust in the South Island to deep sedimentary basins in Cook Strait.

661 7.4 Taupō Volcanic Zone velocity anomalies

The central TVZ, located between the Taupō and Okataina calderas, is an exceptionally productive region of silicic volcanism, while andesitic volcanism is dominant to the north and south (Figure 16A; Wilson et al., 2009). The final velocity model features a low-velocity zone ($V_s<3$ km/s) extending from Ruapehu to White Island in a northeast–southwest trend, bounded by high velocities on either side ($V_s>3.25$ km/s; Figure 16A). Broad-scale velocity features in the TVZ correlate well with spatial boundaries related to geophysical and volcanic domains defined in previous studies.

The Young TVZ is denoted by the solid black lines in Figure 16A and defines a region where intense volcanic and geothermal activity has occurred in the last 350-61 kyr (Wilson et al., 1995). The Young TVZ best outlines the lowest velocities ($V_s<2.75$ km/s) seen in this region. Negative gravity anomalies in the TVZ have been inferred to correlate with collapse areas and large caldera complexes (purple outlines in Figure 16A; Stagpoole et al., 2020), and the individual low-velocity lobes seen within the Young TVZ may represent the juxtaposition of caldera infills and exposed basement rocks. Geothermal fluids within the crust may also explain these low-velocity features which is supported by active geothermal production in the central TVZ (Chambefort et al., 2014). The old TVZ (dashed black line in Figure 16A; Wilson et al., 1995) defines the region of active volcanism in the last 2 My. and captures the general low-velocity zone that extends beyond the Young TVZ ($V_s<3.25$ km/s), while the triangular shaped region of previously-noted positive gravity anomalies (white dashed line in Figure 16A; Stern, 1985), known as the Central Volcanic Region (CVR), corresponds well with the high-velocity V-shape bounding the low velocities here.

We perform a point spread test for one of the shallow, low-velocity lobes within the TVZ (Figure 16C, D). The recovered PSF shows extensive lateral smearing along-rift, offering both caution and guidance in interpreting features here. One peak of the PSF is located near the input perturbation, however high PSF amplitudes can also be seen below White Island, and along the western edge of the TVZ (Figure 16C). This suggests that strong heterogeneities within the TVZ may consequently map to structure offshore, and outside of the volcanic region. This is reinforced in cross-section (Figure 16D), where the lateral uncertainty is evident in the separation of the input perturbation and the recovered PSF. The perturbation is resolved almost 20 km northeast of its actual location, suggesting that resolution of features in the TVZ may have high spatial uncertainty.

At depth, previous geophysical studies have imaged a high-conductivity, plume-like structure beneath the rift axis between Taupō and Okataina (Heise et al., 2010), and low Q_s values underlying caldera structures in the central rift structure (Eberhart-Phillips, Bannister, & Reyners, 2020). We use V_p/V_s to explore the TVZ at depth due to its sensitivity to fluids (Figure 16B). In volcanic regions, high V_p/V_s ratios can be linked to the presence of geothermal fluids or partial melt in the crust (e.g., Husen et al., 2004), while low V_p/V_s have been linked to the presence of a substantial amount of free quartz in basement rock (Ukawa & Fukao, 1981; Christensen, 1996) or gaseous pore fluids in the crust (e.g., Husen et al., 2004).

703 A rift-parallel V_p/V_s cross section shows heterogeneous V_p/V_s structures in the
 704 TVZ that appear to spatially correlate with the varying types of volcanism here (Fig-
 705 ure 16B). To the south, columns of high V_p/V_s (> 1.8) are imaged rising up to the an-
 706 desitic Ruapehu and Tongariro volcanos. These may represent a blurred, long-wavelength
 707 image of distributed melt pockets feeding these volcanoes from depth (Figure 16B). In
 708 contrast, we image shallow (> 8 km), low V_p/V_s (< 1.6) features below the gas-rich
 709 silicic Taupō caldera and northeast of Okataina caldera (Figure 16B). Previous studies
 710 suggest that large melt chambers exist below these active rhyolitic calderas (e.g., S. Barker
 711 et al., 2020; Illsley-Kemp et al., 2021), however we would expect regions of partial melt
 712 to exhibit high, not low, V_p/V_s signatures. The presence of gas at depth has been used
 713 to explain such low- V_p/V_s values (e.g., Husen et al., 2004), and may offer one potential ex-
 714 planation in which gas released by rhyolitic melt at depth fills the pore space above the
 715 inferred melt chambers, leading to the low- V_p/V_s anomalies we image.

716 A PSF for the Taupō caldera shows that recovery of a positive velocity perturba-
 717 tion below lake Taupō results in slightly offset but relatively constrained recovery, sug-
 718 gesting this low- V_p/V_s feature is moderately well resolved. In contrast, the PSF nearby
 719 Okataina caldera (Figure 16D) suggests that an anomaly below the caldera will not be
 720 resolved in the correct location, providing a possible explanation for the high- V_p/V_s sig-
 721 nature located northeast of, rather than directly below, Okataina caldera.

722 7.5 Implications of strong velocity changes

723 The large ($\pm 30\%$) recovered velocity changes with respect to the initial NZ-Wide2.2
 724 velocity model may have significant impacts on studies that rely on 3D velocity struc-
 725 tures as input, such as inversions of shallow subduction slow slip events, earthquake re-
 726 locations, ground motion prediction simulations, and estimations of seismic hazard.

727 Using the NZ-Wide velocity model, Williams and Wallace (2018) generated Green's
 728 functions and estimated the magnitude of slow slip events on the Hikurangi subduction
 729 interface. They found that introducing heterogeneous elastic properties has significant
 730 effects with respect to a homogeneous interface, increasing seismic potency by 58% or
 731 more. Our revised V_s model constitutes heterogeneous changes in elastic properties that
 732 would in-turn have an effect on slip estimations. For example, V_s changes as much as
 733 $\pm 30\%$ would result in almost $\pm 70\%$ change in the shear modulus. These changes are on
 734 par with differences between homogeneous and heterogeneous velocity models presented
 735 in Williams and Wallace (2018). Increased offshore resolution of the shallow subduction
 736 interface should also increase heterogeneity of interface properties, leading to greater spa-
 737 tial variations in estimations of expected slip.

738 Earthquake relocation is an important method for constraining relative or abso-
 739 lute locations of seismic events. Relocated earthquake catalogs can be used to map fault
 740 structures (e.g., Lanza et al., 2019), infer pore fluid pressures, or spatially constrain large-
 741 scale tectonic features (e.g., Reyners et al., 2017). Methods like nonlinear location in-
 742 version (Lomax et al., 2000) rely on input 3D velocity models to search for optimum earth-
 743 quake locations and consequently the NZ-Wide velocity model has been employed in New
 744 Zealand earthquake relocation studies (e.g., Bannister et al., 2011; Reyners et al., 2011;
 745 Lanza et al., 2019). We would expect changes introduced in this velocity study to affect
 746 inferred earthquake locations. For example, revised offshore velocities should improve
 747 locations of near-offshore earthquakes, while increased resolution of crustal structure may
 748 help constrain depths of shallow earthquakes.

749 Ground motion simulations can be used to constrain expected ground shaking for
 750 large potential earthquakes (e.g., Graves et al., 2011; Bradley et al., 2017). In these sim-
 751 ulations, the underlying velocity model controls 3D wave propagation effects, such as am-
 752 plified shaking in sedimentary basins or directivity caused by topography or subsurface
 753 structure. In the South Island, New Zealand, for example, ground motion simulations

of a large Alpine fault rupture show significant rupture directivity and basin-generated surface waves that result in notable increases in peak ground velocities (Bradley et al., 2017). Similarly, velocity models in southern California have been used to constrain strong ground motion of potential fault ruptures to estimate seismic hazard (Graves et al., 2011).

Our updated velocity model, resultant wave propagation simulations, and predictions of faults and ground shaking, will impact the estimation of seismic hazards in New Zealand. For example, observed long-duration ground shaking in offshore regions should be more accurately captured by the updated velocity structures (Kaneko et al., 2019). Similarly, Ellis et al. (2017) show that velocity gradients at depth can be used to identify previously unmapped faults which may host large, damaging earthquakes. Improved crustal resolution in our velocity model should assist in such studies which make use of 3D velocity structures.

8 Conclusions

We perform 28 L-BFGS iterations to improve a starting 3D velocity model of the North Island of New Zealand using spectral element and adjoint methods. Waveforms for 60 events recorded on up to 88 broadband seismic stations are compared with synthetic waveforms within automatically selected time windows and quantified using a traveltimes cross-correlation objective function. Measurements are made on up to 1800 source-receiver pairs, for a final waveform period range of 4–30 s. Computational cost totalled ~500 000 CPU-hours over the course of the inversion.

The final velocity model (M28) is defined by updated V_p and V_s . Net model updates show large—up to $\pm 30\%$ —heterogeneous velocity changes with respect to the initial V_s model. In general, velocities are slowed down, existing features are sharpened, and new velocity anomalies are imaged. Resolution analyses using point spread function and a zeroth moment test show that model updates are resolved best in terms of V_s , on land and in the near-offshore region, and above ~ 30 km depth. Comparisons with geologic cross sections (Figure 13) show that the final model is able to resolve shallow velocity structure (> 5 km depth). Point spread functions used to test robustness of individual features in the final velocity model show varying degrees of resolution.

We interpret the most striking velocity changes in the context of known geology and tectonics. Shallow V_s velocity structures correlate well with New Zealand basement terranes, and sedimentary and volcanic cover. Along-strike V_p/V_s structures show increased heterogeneity that contrasts with previous interpretations in which heterogeneous terrane permeability controls interface locking. In Cook Strait we image steep-sided, deep sedimentary basins as strong velocity contrasts between Cook Strait and the North and South Islands. In the Taupō Volcanic Zone we image slow, shallow velocities at the surface that generally correlate with low-gravity anomalies inferred as caldera locations, as well as heterogeneous V_p/V_s structures at depth that show good correlation with observed volcanic compositions.

The velocity models presented in this study provide further constraint on enigmatic tectonic properties of the Hikurangi Subduction Zone. New Zealand source–receiver coverage ultimately limits the resolving power of our methods, and future work may target improved resolution through denser, more uniform receiver coverage. Additionally, more focused efforts to fit short-period (~ 2 s) waveforms, for example through careful curation of input data, may improve resolution of short-wavelength (< 5 km) features. New Zealand velocity models, as derived in this study, are important for understanding Earth structure and have first-order impact on other work including earthquake relocations, megathrust slip research, and estimations of seismic hazard.

802 Open Research

803 Temporary network seismic waveform datasets used in this research are available
804 in these intext data citation references: Bannister (2009), Bannister and Bourguignon
805 (2011), Henrys et al. (2013), Kaneko and Chow (2017).

806 The final M28 velocity model and associated metadata is publicly available through
807 a public repository (<https://core.geo.vuw.ac.nz/d/feae69f61ea54f81bee1/>). BEACON de-
808 ployment continuous waveform data and metadata are available through IRIS (Kaneko
809 & Chow, 2017). Waveform data from the New Zealand permanent network (GeoNet) and
810 the SAHKE deployment were accessed publicly via IRIS FDSN webservices.

811 Acknowledgments

812 This work was funded by a Rutherford Discovery Fellowship and Marsden Fund awarded
813 by the Royal Society of New Zealand. We thank Donna Eberhart-Phillips for providing
814 the latest NZ-Wide2.2 3D velocity model. We acknowledge John Ristau for providing
815 earthquake moment tensors. BEACON field deployment and servicing was performed
816 by: Yoshihiro Kaneko, Bryant Chow, Jonathan Hanson, Dan Whitaker, Rory Hart, Con-
817 rad Burton, Garth Archibald, Dan Bassett, Kris O'Brien, Tim McDougall, Hubert Zal,
818 Danielle Lindsay, and Jesse Kearse. All simulation work was performed on the New Zealand
819 eScience Infrastructure's HPC, Maui. We thank Alexander Pletzer for helping us op-
820 timize SPECFEM3D Cartesian on Maui. We thank Finnigan Illsley-Kemp, Calum Cham-
821 berlain, Laura Wallace, Susan Ellis, Tim Little and Carolyn Boulton for fruitful discus-
822 sions during interpretations of the final velocity model.

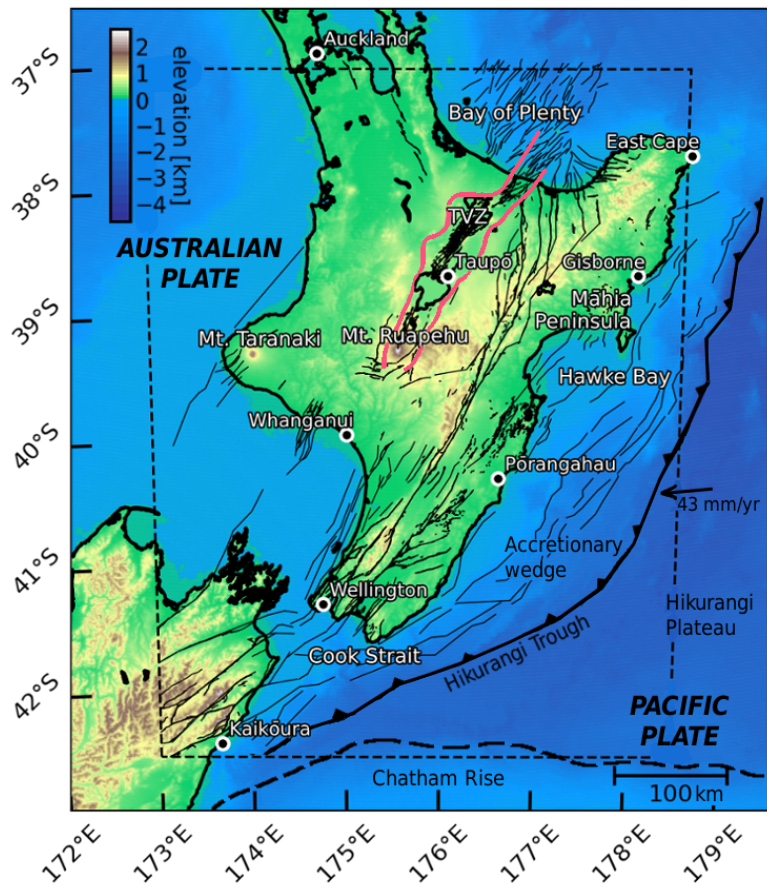


Figure 1. Tectonic setting for the North Island of New Zealand. New Zealand active onshore and offshore faults plotted as thin black lines (Litchfield et al., 2014). The thick, dashed, black line shows the continent-ocean boundary between the Chatham Rise and the Hikurangi Plateau. Elevation values are defined by SRTM-30P (Becker et al., 2009), which are also used to define topography and bathymetry for the numerical mesh. Geographic and tectonic landmarks are labelled, with select towns and cities marked by black circles. The solid red lines show the outline of the Taupō Volcanic Zone (TVZ). The tomographic simulation domain is shown by the thin, dashed, black outline.

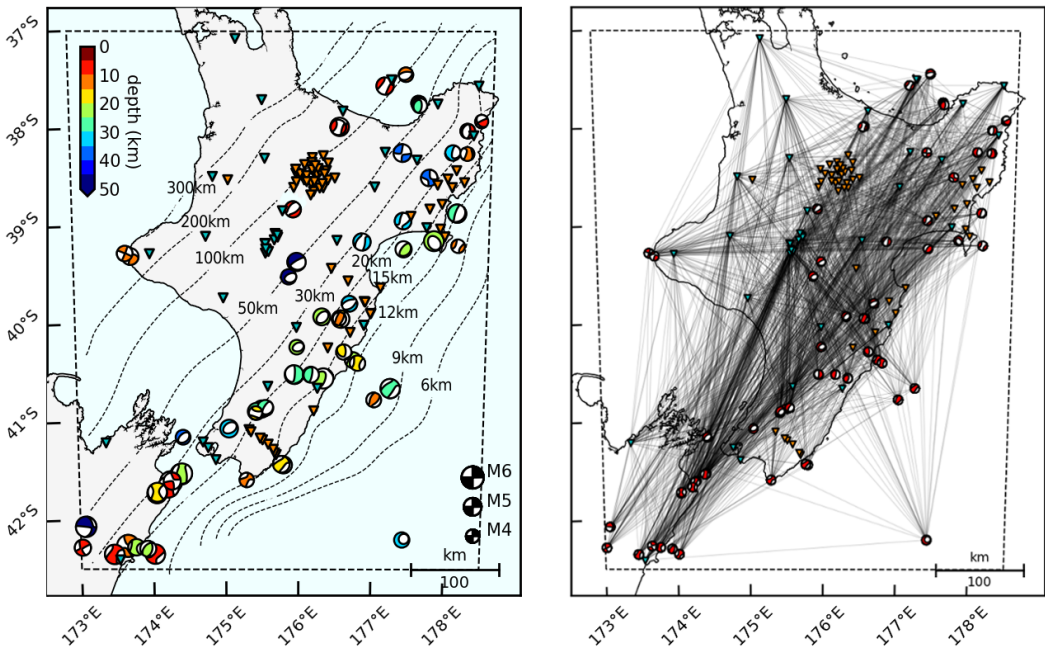


Figure 2. Sources and receivers included in the inversion. Left: 60 earthquakes shown as focal mechanisms, color coded by depth, and scaled by magnitude. 88 broadband seismic stations shown as inverted triangles, with 38 permanent network (GeoNet) stations colored blue, and 50 temporary network stations colored orange. Plate interface model of Williams et al. (2013) shown as dashed contour lines. Right: Source–receiver ray paths for the first iteration of the inversion. Sources and receivers same as in (A). Connecting raypaths only shown for sources and receivers that have at least one measurement window.

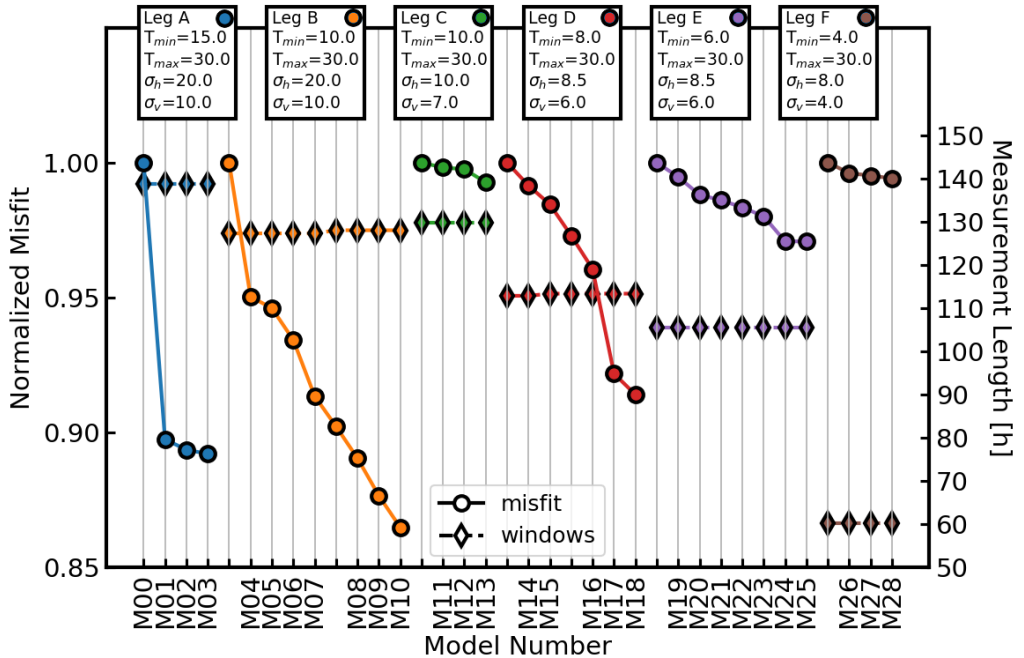


Figure 3. Convergence plot which shows reduction of waveform misfit over the course of the inversion. Each line represents an individual inversion leg. Bandpass (T) and horizontal and vertical standard deviations of the 3D Gaussian used for gradient smoothing (σ) are annotated above each leg. Misfit (Equation 2) is plotted as circles and normalized to the starting misfit of each given inversion leg. Diamonds show cumulative window length in hours. Adjacent points that share a model number (e.g., at the transition between inversion legs) correspond to re-evaluation of the misfit using the same model, for example through re-selection of time windows or through a change of inversion parameters.

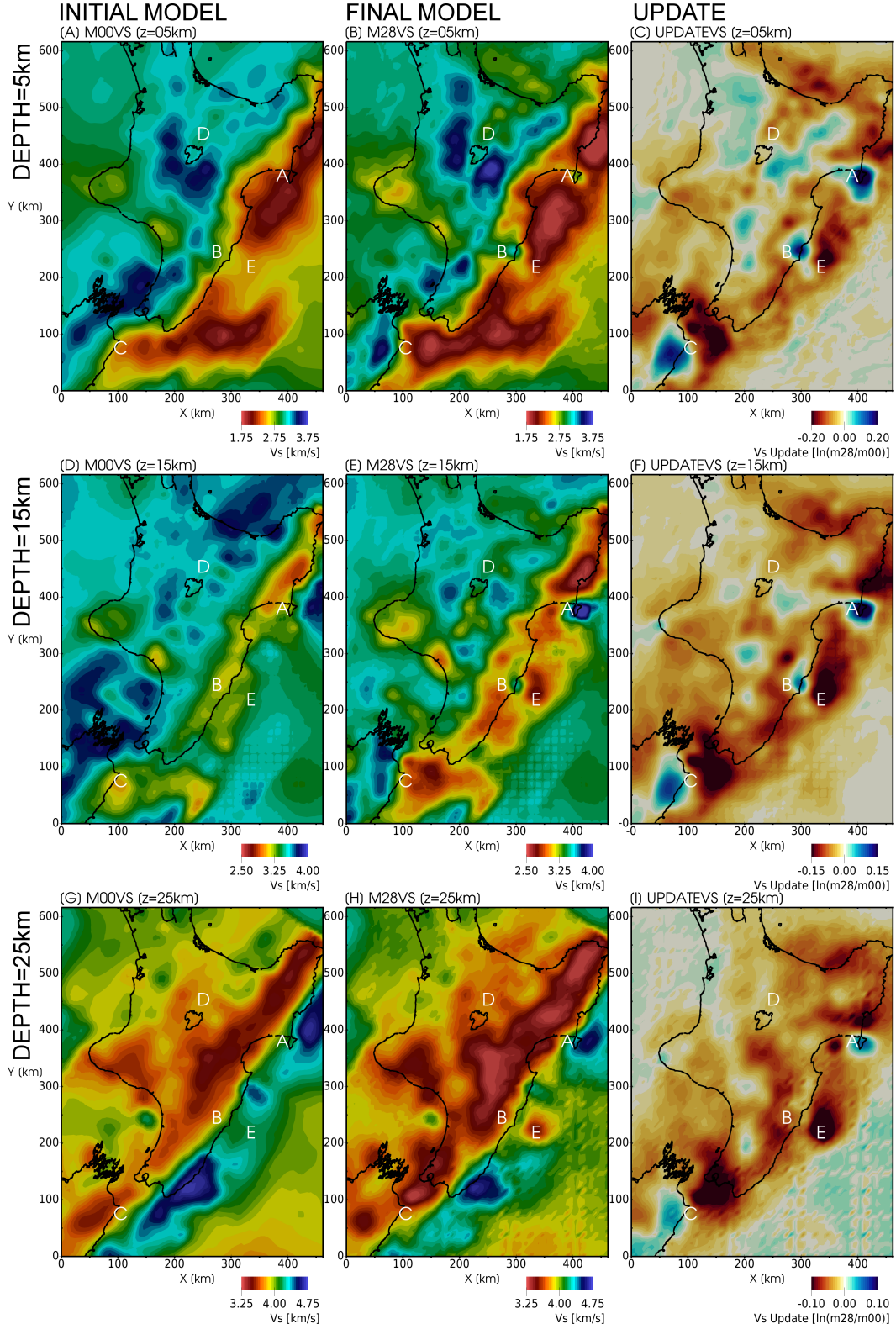


Figure 4. Comparisons of initial (M00) and final (M28) V_s velocity models at various depth slices. Columns represent initial model (M00; left), final model (M28; center), and net model update ($\ln(M28/M00)$; right). Rows represent depth slices at 5 km (top), 15 km (middle), and 25 km (bottom). Annotated letters A–E relate to notable features discussed in Section 5. Note the differing color scales between rows and columns. Numerical artefacts related to mesh coarsening layers (Section 5.1) are visible in panels D, E, F, H, and I.

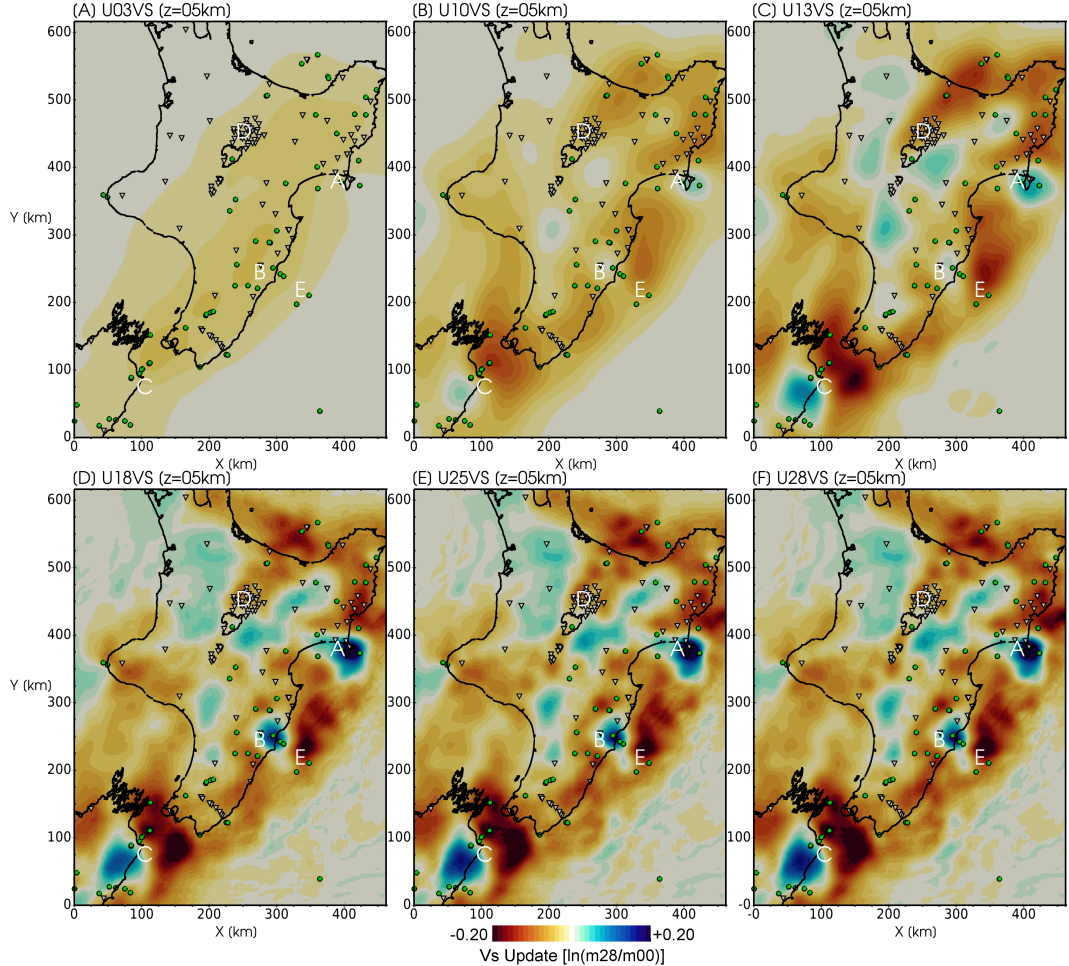


Figure 5. V_s net model updates at 5 km depth for the final iteration of each inversion leg (Figure 3). Features A–E are the same as in Figure 4. The color scale is the same for each figure, at ± 0.20 , or approximately $\pm 20\%$ velocity change. Note that the color scale saturates, and maximum velocity changes by M28 are as much as $\pm 30\%$. Source locations are depicted by green dots; station locations are depicted by inverted triangles.

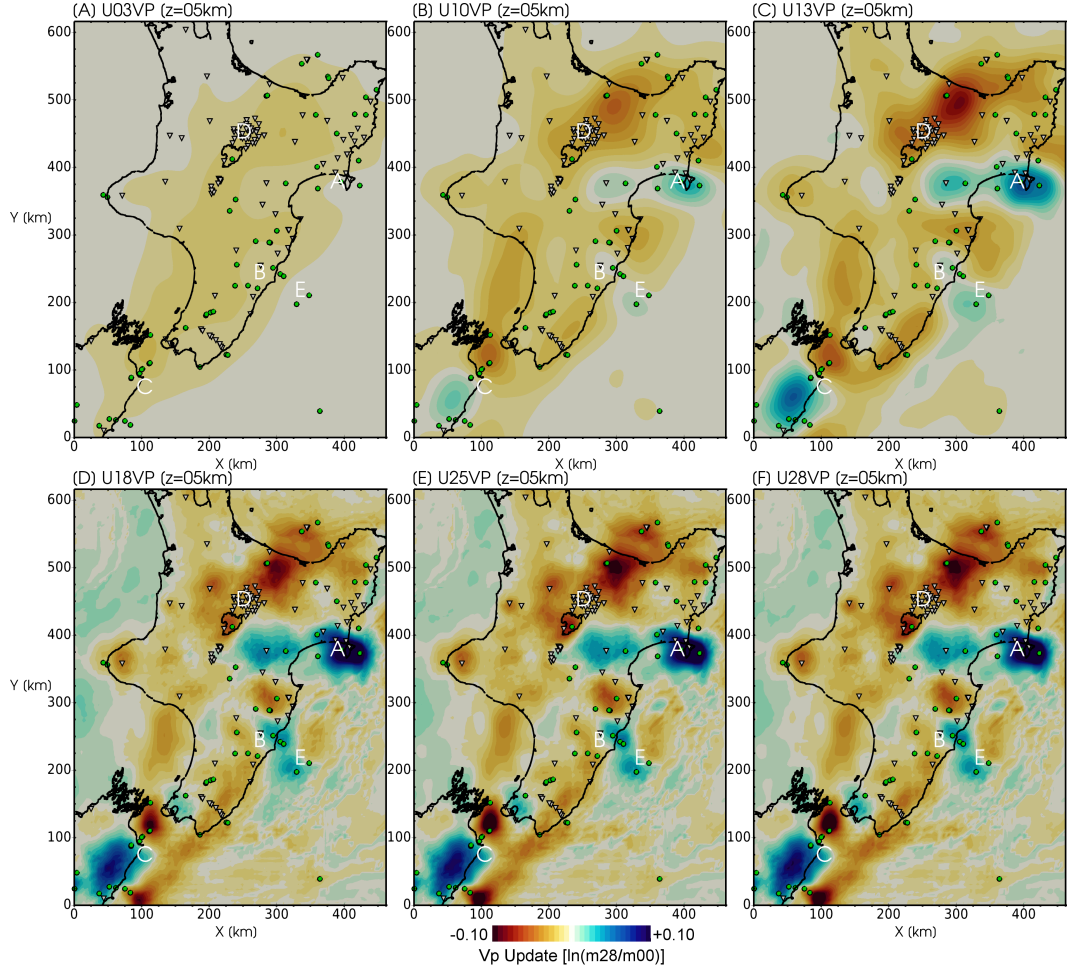


Figure 6. V_p net model updates at 5 km depth for the final iteration of each inversion leg (Figure 3). Features A–E are the same as in Figure 4. The color scale is the same for each figure, at ± 0.10 , or approximately $\pm 10\%$ velocity change. Note that the color scale saturates, and maximum velocity changes by M28 are as much as $\pm 25\%$. Source locations are depicted by green dots; station locations are depicted by inverted triangles.

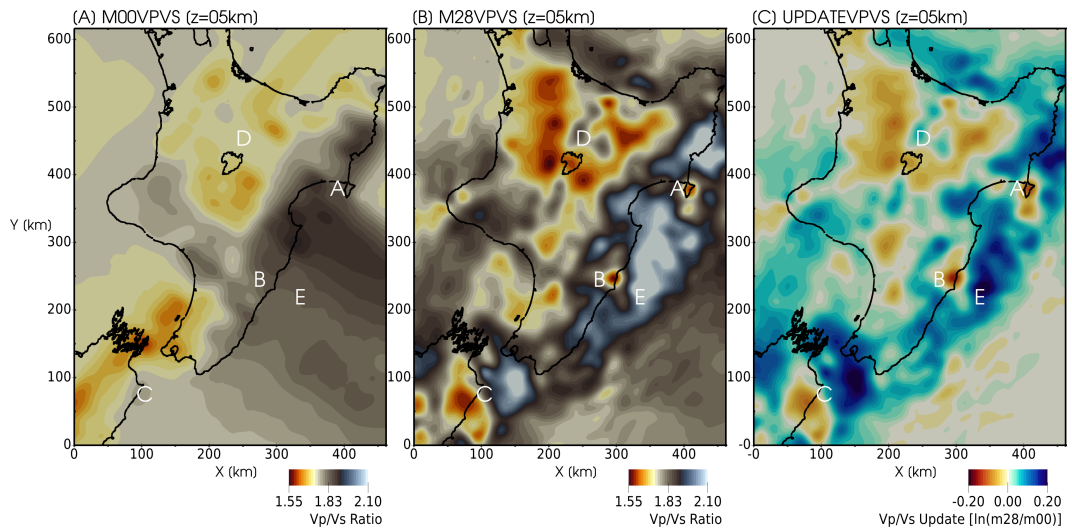


Figure 7. Comparisons of V_p/V_s ratio at 5 km depth. The V_p/V_s ratio for a Poisson's solid ($V_p/V_s = 1.73$) corresponds to white colors. A) Initial model (M00) at 5 km depth. B) Final model (M28) at 5 km depth. C) Net model update $\ln(M28/M00)$ at 5 km depth. Labels A–E relate to features discussed in Section 5 and shown in Figure 4.

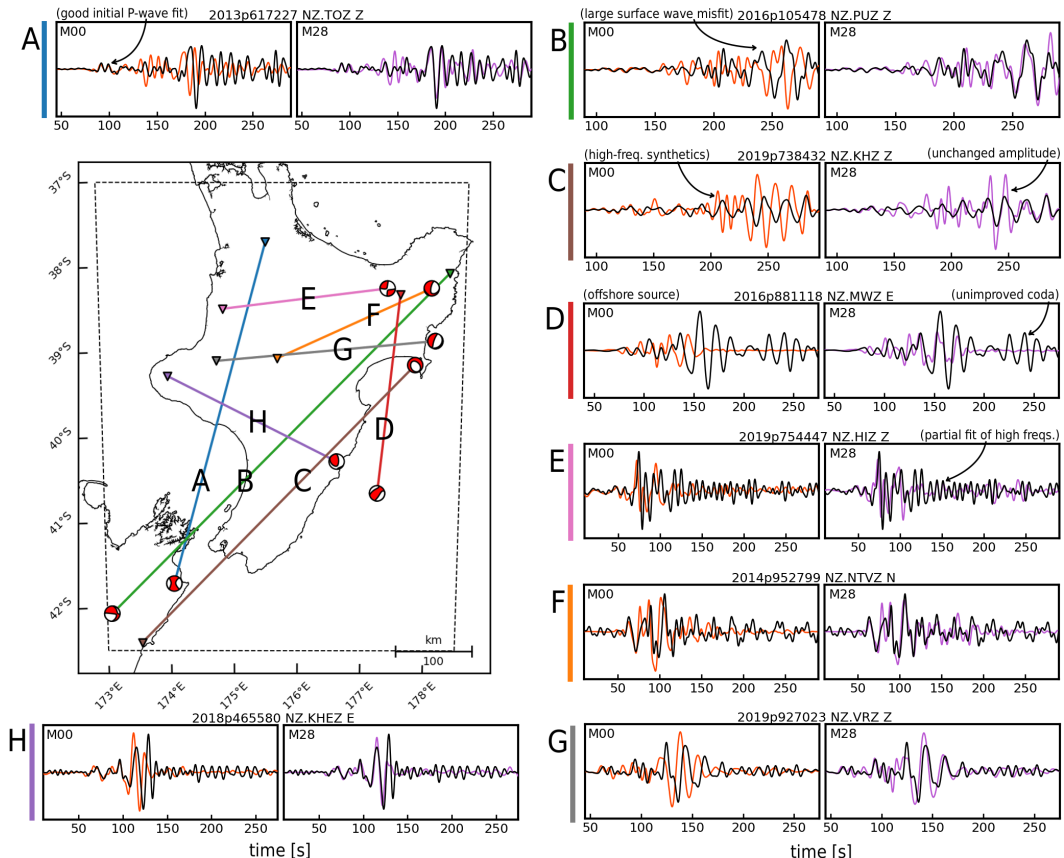


Figure 8. Waveform comparisons for eight unique source–receiver pairs. Each comparison (A–H) consists of two panels showing data (black) and synthetics for the initial model (M00; red) and final model (M28; purple). All waveforms are processed and filtered identically within a bandpass of 6–30 s. The map shows corresponding moment tensors, receiver locations, and ray-paths. GeoNet earthquake event ID, station code, and waveform component are annotated in the title of each panel. Select waveforms are annotated based on corresponding text in Section 5.3, with freq. as a shorthand for frequency. Waveforms are shown in units of displacement [m].

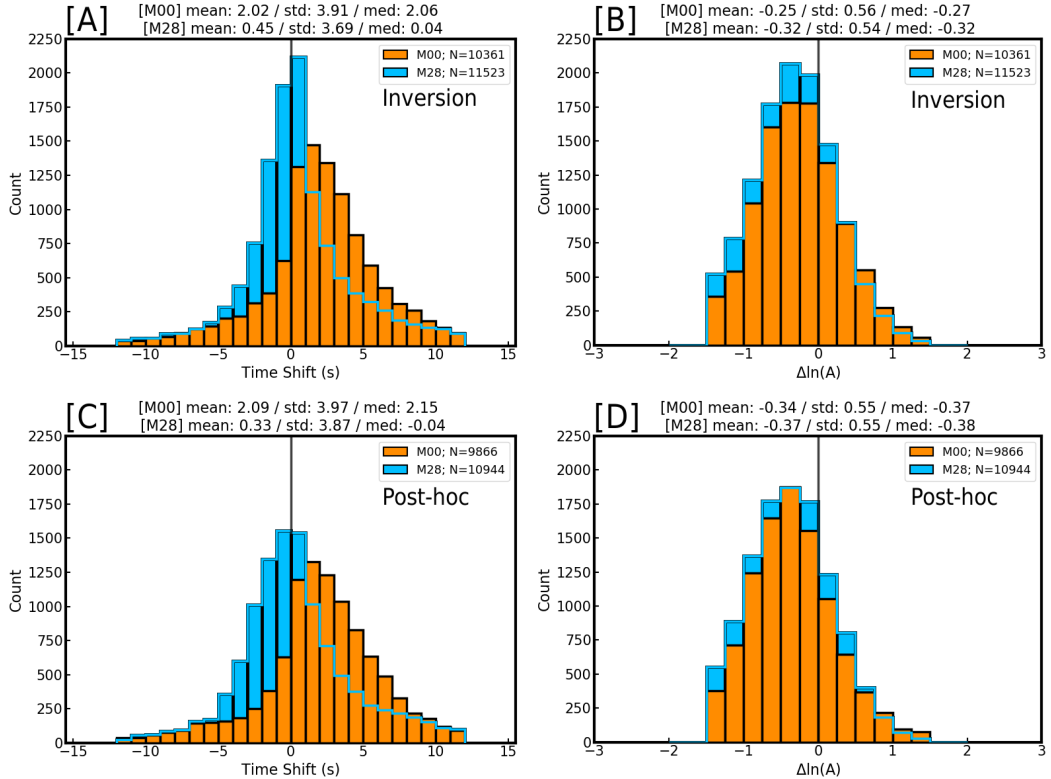


Figure 9. Misfit histograms detailing bulk misfit assessment between the initial model (M00; orange), and final model (M28; blue) for 60 events used in the inversion (top) and a separate 60 event post-hoc validation catalog (bottom). All histograms are based on 6–30 s waveforms. Mean, standard deviation, and median values for each respective histogram are given in the title of each figure. The number of measurements for each histogram is provided in the respective legends. Amplitude difference is defined as $\Delta \ln A = \ln[\int d^2(t)dt / \int s^2(t)dt]$, where d and s are observed and synthetic waveforms. A) Time shift for inversion events. B) Amplitude difference for inversion events. C) Time shift for post-hoc events. D) Amplitude difference for post-hoc events.

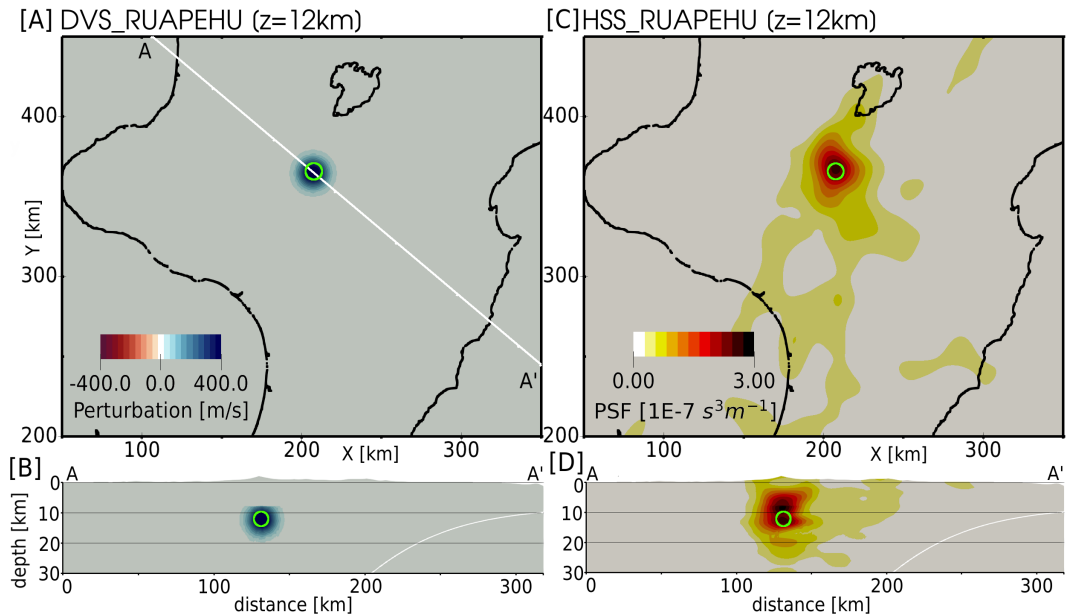


Figure 10. An example point spread function (PSF). A, B) 3D spherical Gaussian velocity perturbation placed at 12 km depth. The peak amplitude of the perturbation is 15% of the final V_s velocity model. The horizontal and vertical full-widths of the perturbation (green circles) are 10 km and 5 km, respectively. C, D) Recovered PSF illustrating how the perturbation is smeared by the inversion procedure. A–A' cross sections are shown at 2x vertical exaggeration. White lines in cross sections correspond to the plate interface model of Williams et al. (2013).

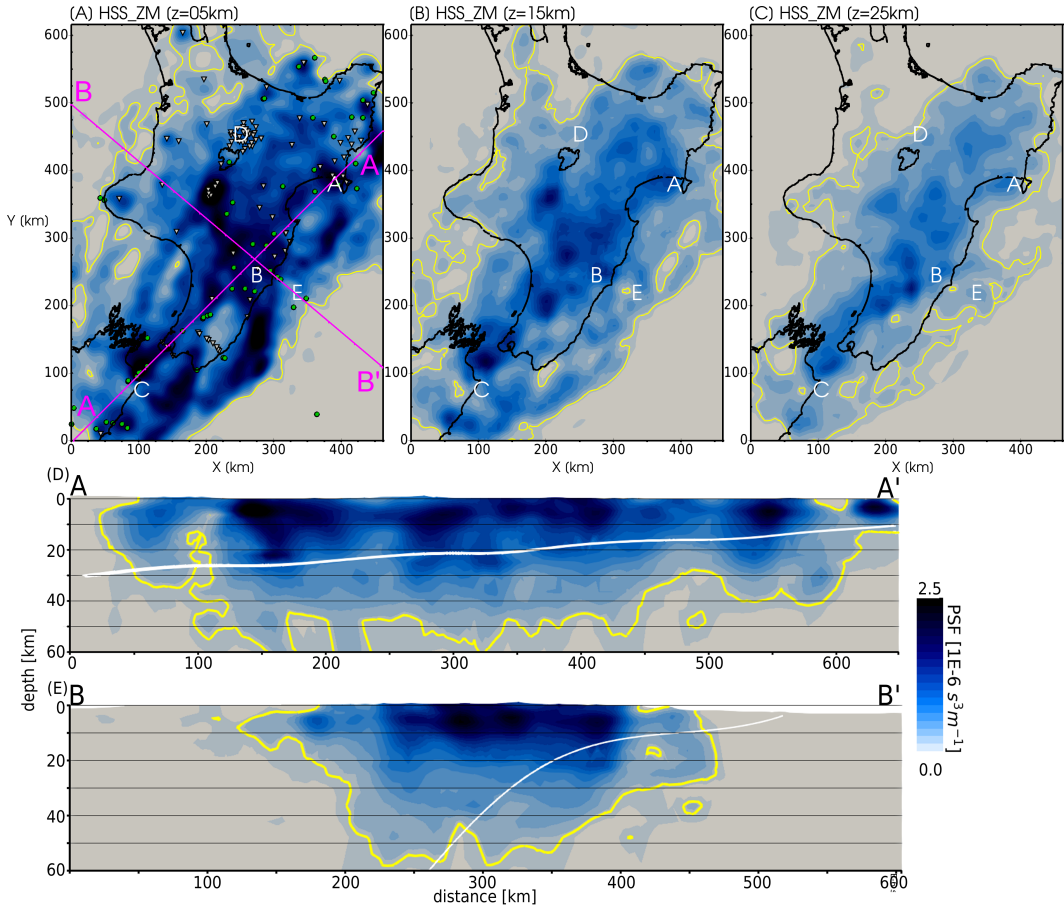


Figure 11. Zeroth moment test showing relative weight of point spread functions for a homogeneous 50 m/s V_s perturbation with respect to the final velocity model. The volumetric field approximates the sensitivity of the entire set of waveform measurements to perturbations in V_s structures. Solid yellow lines outline a threshold value of $2.5 \times 10^{-7} \text{ s}^3 \text{ m}^{-1}$. A) H_{SS} at 5 km depth. Pink lines show surface traces of cross sections in (D) and (E). Earthquakes and receivers used in inversion are depicted as green circles and white inverted triangles. B) H_{SS} at 15 km depth. C) H_{SS} at 25 km depth. D) H_{SS} A–A' cross section to 60 km depth at 2x vertical exaggeration. E) H_{SS} B–B' cross section. White lines in cross sections correspond to the plate interface model of Williams et al. (2013).

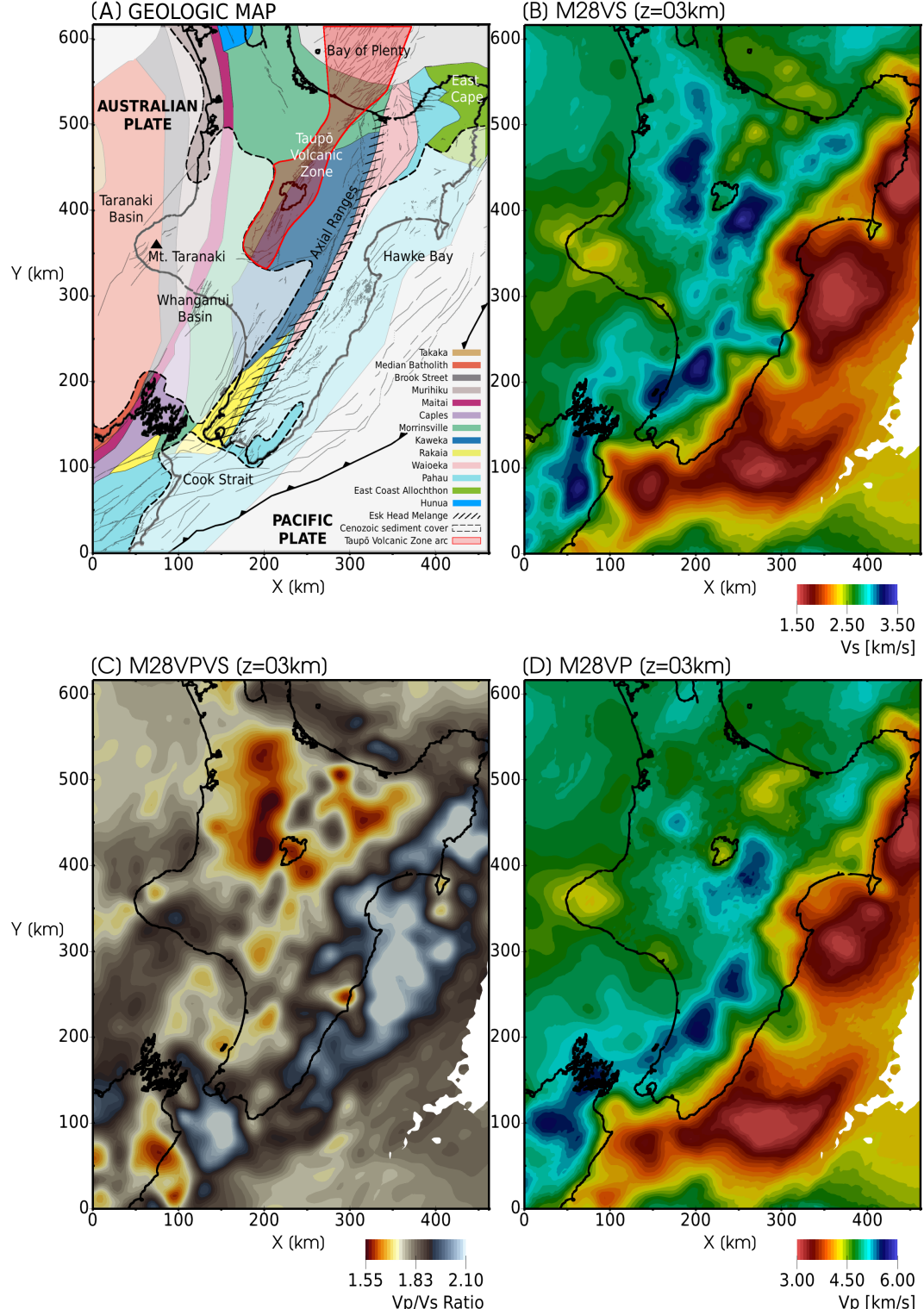


Figure 12. A comparison of New Zealand geology (Mortimer, 2004; Edbrooke et al., 2015) and the final velocity models (M28) at 3 km depth. A) Thin gray lines show active faults (Litchfield et al., 2014). B) M28 V_s . C) M28 V_p/V_s . D) M28 V_p . The white region on the right side of the velocity models corresponds to bathymetry deeper than 3 km, and therefore no velocity values are available.

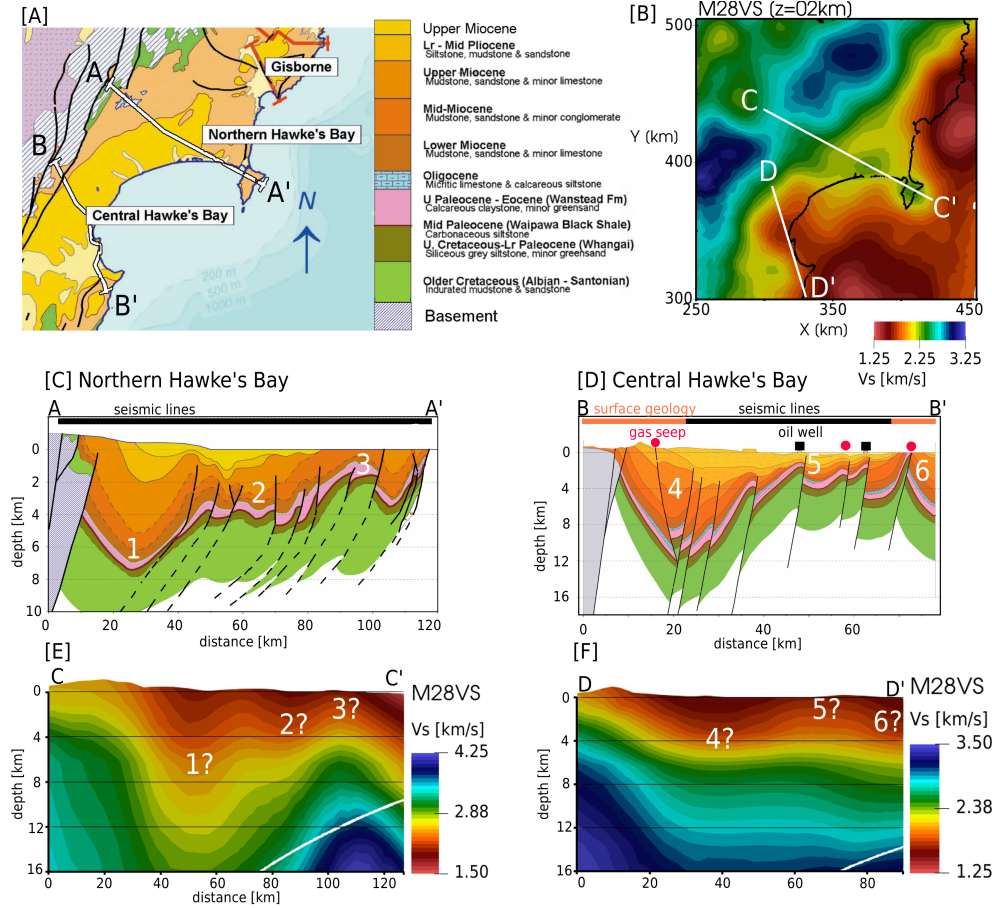


Figure 13. Geologic cross sections of Francis et al. (2004) compared with the final V_s velocity model (M28). A) Map view of the Hawke's Bay region. Colors correspond to sedimentary rock types in the legend. A–A' and B–B' show surface traces of cross sections shown in (C) and (D). B) 2 km depth slice of M28 V_s model. C–C' and D–D' corresponds to surface traces of cross sections shown in (E) and (F). C) A–A' geologic cross section through Northern Hawke's Bay at 5x vertical exaggeration. Features 1, 2, and 3 used for comparisons with the velocity model in (E). Black lines represent faults, with dashed lines referring to inferred fault continuations. This cross section is interpreted from active source seismic data. D) B–B' Central Hawke's Bay geologic cross section at 2X vertical exaggeration, derived from surface geology and seismic lines. Gas seeps and oil well locations are shown as red circles and black squares. Features 4, 5, and 6 correspond to features in (F). E) C–C' cross section through M28 V_s model at 4x vertical exaggeration. White solid line shows the plate interface model of Williams et al. (2013). Corresponding velocity features 1, 2, and 3 are from (C). F) D–D' cross section through M28 V_s model at 3x vertical exaggeration. Corresponding velocity features 4, 5, and 6 are from (D).

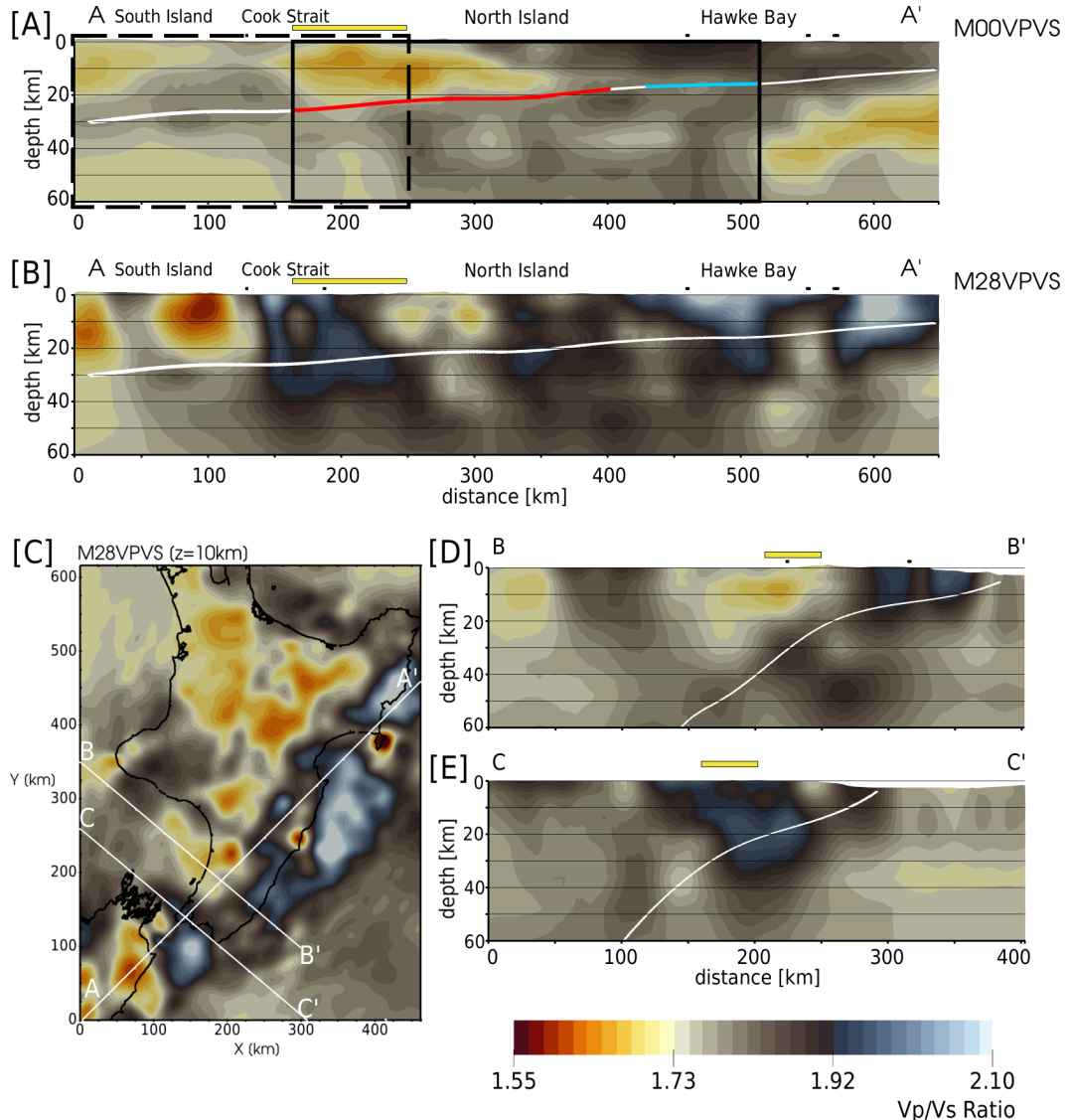


Figure 14. Along-strike heterogeneity of V_p/V_s represented by three vertical cross sections (A–A', B–B', C–C') whose lines are shown in (C). Cross sections are shown to 60 km depth with 2x vertical exaggeration; solid white line corresponds to the plate interface model of Williams et al. (2013); solid yellow line shows the approximate location of Rakaia terrane (Figure 12A). A) M00 V_p/V_s A–A' cross section. Black outlines correspond to approximate bounds of Figure 5 (solid) and Figure 6 (dashed) of Reyners et al. (2017). Approximate geographic locations are annotated above the plot. Red interface line marks where slip rate deficit is > -20 mm/yr. Blue line marks where slip rate deficit is < -10 mm/yr (Wallace, Barnes, et al., 2012; Reyners et al., 2017). B) M28 V_p/V_s A–A' cross section. C) M28 V_p/V_s at 10 km depth. D) M28 V_p/V_s B–B' cross section. E) M28 V_p/V_s C–C' cross section.

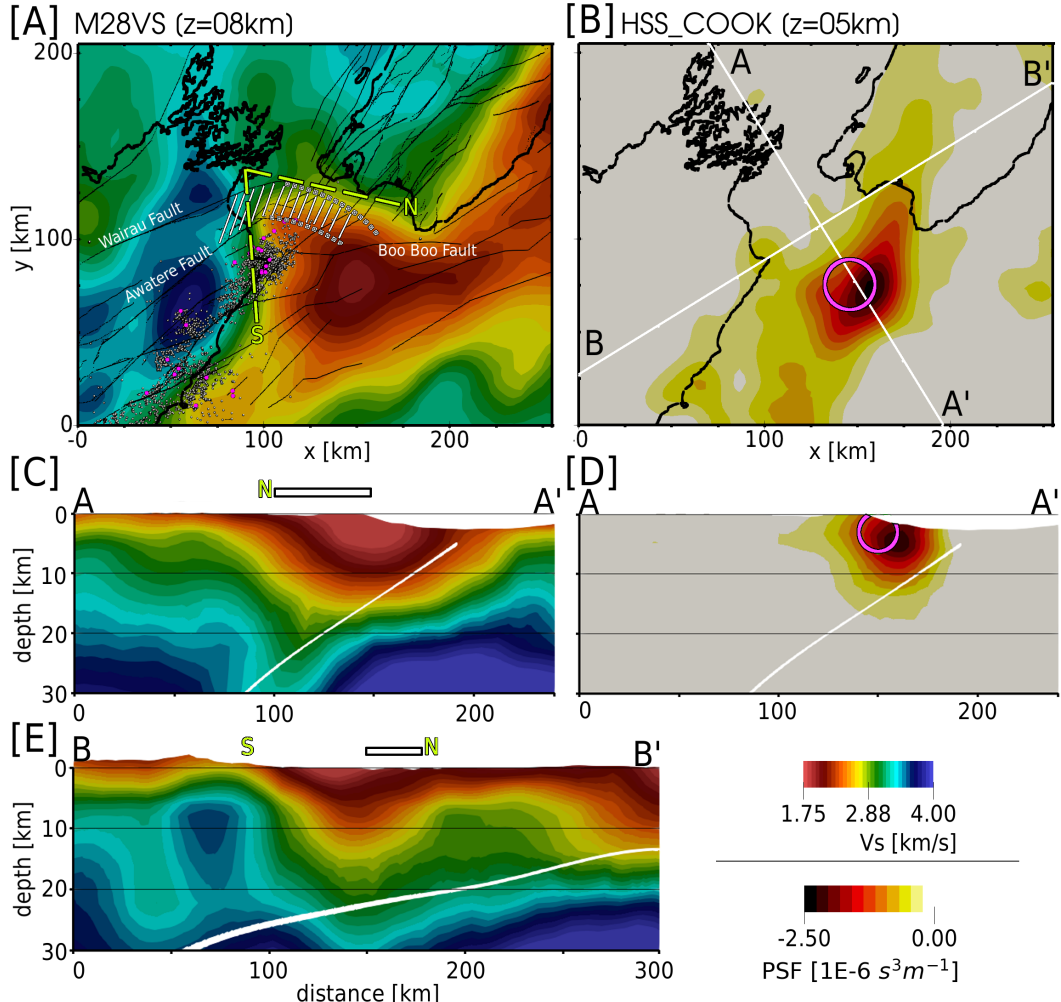


Figure 15. Cook Strait velocity gradient and point spread test. A) M28 V_s at 8 km depth. Northern (N) and southern (S) velocity gradients are marked by green dashed lines. Relocated Kaikōura aftershocks with depth > 20 km and $M > 3$ are shown as white circles (Chamberlain et al., 2021). Earthquakes $M > 5.5$ are colored pink (GeoNet). The crustal transition zone (CTZ) identified by Henrys et al. (2020) is marked by the hatched pattern. B) PSF at 5 km depth. Horizontal full width of input Gaussian perturbation is shown as an open pink circle. Surface traces A–A' and B–B' correspond to cross sections in C–E. C) M28 V_s A–A' cross section. Locations of northern velocity gradient (N) and CTZ are marked. D) H_{ss} A–A' cross section. Vertical full width of input Gaussian perturbation is shown as the open pink circle. E) M28 V_s B–B' cross section. Locations of northern velocity gradient (N), southern velocity gradient (S), and CTZ are marked. All cross sections shown with 3x vertical exaggeration. White solid lines denote the plate interface model of Williams et al. (2013).

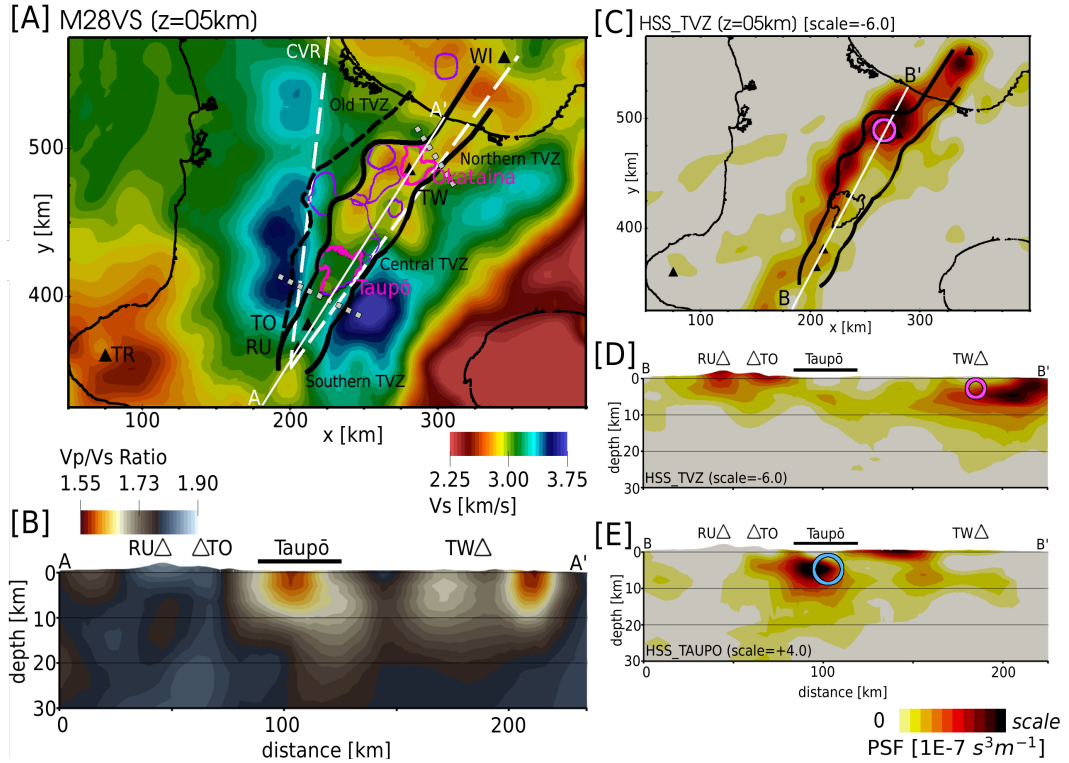


Figure 16. Taupō Volcanic Zone (TVZ) velocity anomalies and point spread test. A) M28 V_s at 5 km depth. Solid black lines mark the extent of the Young TVZ, separated into southern, central, and northern segments (gray dotted lines). Dashed black line shows the western boundary of the Old TVZ, which shares its eastern boundary with the Young TVZ. The white dashed lines show the Central Volcanic Region (CVR). Black triangles mark locations of volcanoes discussed in text (TR: Taranaki, RU: Ruapehu, TO: Tongariro, TW: Tarawera, WI: White Island). Purple lines show locations of low gravity velocity anomalies that correlate with topographic extents of geologically inferred calderas (Stagpoole et al., 2020). B) M28 V_p/V_s A–A' cross section. C) PSF at 5 km depth for a negative velocity perturbation placed within the TVZ. The horizontal full width of the input perturbation is denoted by the open pink circle. D) PSF B–B' cross section, same as in (C). E) PSF B–B' cross section for a positive-velocity perturbation at 5 km depth below lake Taupō (blue circle).

823 References

- Audet, P., Bostock, M. G., Christensen, N. I., & Peacock, S. M. (2009). Seismic evidence for overpressured subducted oceanic crust and megathrust fault sealing. *Nature*, 457(7225), 76–78.
- Bannister, S. (2009). *Deep Geothermal HADES seismic array*. International Federation of Digital Seismograph Networks. Retrieved from http://www.fdsn.org/networks/detail/Z8_2009/ doi: 10.7914/SN/Z8_2009
- Bannister, S., & Bourguignon, S. (2011). *Gisborne-Mahia Seismic Tremor Array*. International Federation of Digital Seismograph Networks. Retrieved from http://www.fdsn.org/networks/detail/ZX_2011/ doi: 10.7914/SN/ZX_2011
- Bannister, S., Fry, B., Reyners, M., Ristau, J., & Zhang, H. (2011). Fine-scale relocation of aftershocks of the 22 February Mw 6.2 Christchurch earthquake using double-difference tomography. *Seismological Research Letters*, 82(6), 839–845.
- Barker, D., Sutherland, R., Henrys, S., & Bannister, S. (2009). Geometry of the Hikurangi subduction thrust and upper plate, North Island, New Zealand. *Geochemistry, Geophysics, Geosystems*, 10(2).
- Barker, S., Rowe, M. C., Wilson, C. J., Gamble, J. A., Rooyakkers, S. M., Wysoczanski, R. J., ... Kenworthy, C. C. (2020). What lies beneath? Reconstructing the primitive magmas fueling voluminous silicic volcanism using olivine-hosted melt inclusions. *Geology*, 48(5), 504–508.
- Barnes, P. M., & Audru, J.-C. (1999). Quaternary faulting in the offshore Flaxbourne and Wairarapa basins, southern Cook Strait, New Zealand. *New Zealand Journal of Geology and Geophysics*, 42(3), 349–367.
- Barnes, P. M., Lamarche, G., Bialas, J., Henrys, S., Pecher, I., Netzeband, G. L., ... Crutchley, G. (2010). Tectonic and geological framework for gas hydrates and cold seeps on the Hikurangi subduction margin, New Zealand. *Marine Geology*, 272(1-4), 26–48.
- Becker, J., Sandwell, D., Smith, W., Braud, J., Binder, B., Depner, J., ... others (2009). Global bathymetry and elevation data at 30 arc seconds resolution: SRTM30_PLUS. *Marine Geodesy*, 32(4), 355–371.
- Bell, R., Holden, C., Power, W., Wang, X., & Downes, G. (2014). Hikurangi margin tsunami earthquake generated by slow seismic rupture over a subducted seamount. *Earth and Planetary Science Letters*, 397, 1–9.
- Bozdağ, E., Peter, D., Lefebvre, M., Komatitsch, D., Tromp, J., Hill, J., ... Pugmire, D. (2016). Global adjoint tomography: first-generation model. *Geophysical Journal International*, 207(3), 1739–1766.
- Bradley, B. A., Bae, S. E., Polak, V., Lee, R. L., Thomson, E. M., & Tarbali, K. (2017). Ground motion simulations of great earthquakes on the Alpine Fault: effect of hypocentre location and comparison with empirical modelling. *New Zealand Journal of Geology and Geophysics*, 60(3), 188–198.
- Carter, R. M., & Naish, T. R. (1998). A review of Wanganui Basin, New Zealand: global reference section for shallow marine, Plio-Pleistocene (2.5–0 Ma) cyclostratigraphy. *Sedimentary Geology*, 122(1-4), 37–52.
- Chambefort, I., Lewis, B., Wilson, C., Rae, A., Coutts, C., Bignall, G., & Ireland, T. (2014). Stratigraphy and structure of the Ngatamariki geothermal system from new zircon U–Pb geochronology: Implications for Taupo Volcanic Zone evolution. *Journal of Volcanology and Geothermal Research*, 274, 51–70.
- Chamberlain, C. J., Frank, W., Lanza, F., Townend, J., & Warren-Smith, E. (2021). Illuminating the pre-, co-, and post-seismic phases of the 2016 M7.8 Kaikoura earthquake with 10 years of seismicity.
- Chen, M., Niu, F., Liu, Q., Tromp, J., & Zheng, X. (2015). Multiparameter adjoint tomography of the crust and upper mantle beneath East Asia: 1. Model construction and comparisons. *Journal of Geophysical Research: Solid Earth*, 120(3), 1762–1786.

- 878 Chow, B., Kaneko, Y., Tape, C., Modrak, R., & Townend, J. (2020). An automated
879 workflow for adjoint tomography — waveform misfits and synthetic inversions
880 for the North Island, New Zealand. *Geophysical Journal International*, 223(3),
881 1461–1480.
- 882 Chow, B., Kaneko, Y., & Townend, J. (companion manuscript). Evidence for
883 deeply-subducted lower-plate seamounts at the Hikurangi subduction mar-
884 gin: implications for seismic and aseismic behavior. *Journal of Geophysical*
885 *Research: Solid Earth*.
- 886 Christensen, N. I. (1996). Poisson's ratio and crustal seismology. *Journal of Geo-*
887 *physical Research: Solid Earth*, 101(B2), 3139–3156.
- 888 Cochran, U., Berryman, K., Zachariasen, J., Mildenhall, D., Hayward, B., Southall,
889 K., ... others (2006). Paleoecological insights into subduction zone earthquake
890 occurrence, eastern North Island, New Zealand. *GSA Bulletin*, 118(9-10),
891 1051–1074.
- 892 Collot, J.-Y., Delteil, J., Lewis, K. B., Davy, B., Lamarche, G., Audru, J.-C., ...
893 others (1996). From oblique subduction to intra-continental transpression:
894 Structures of the southern Kermadec-Hikurangi margin from multibeam
895 bathymetry, side-scan sonar and seismic reflection. *Marine Geophysical Re-*
896 *searches*, 18(2), 357–381.
- 897 Dahlen, F., & Baig, A. M. (2002). Fréchet kernels for body-wave amplitudes. *Geo-*
898 *physical Journal International*, 150(2), 440–466.
- 899 Dahlen, F., Hung, S.-H., & Nolet, G. (2000). Fréchet kernels for finite-frequency
900 traveltimes—I. Theory. *Geophysical Journal International*, 141(1), 157–174.
- 901 Darby, D. J., Hodgkinson, K. M., & Blick, G. H. (2000). Geodetic measurement
902 of deformation in the Taupo Volcanic Zone, New Zealand: the north Taupo
903 network revisited. *New Zealand Journal of Geology and Geophysics*, 43(2),
904 157–170.
- 905 Davy, B., Hoernle, K., & Werner, R. (2008). Hikurangi Plateau: Crustal structure,
906 rifted formation, and Gondwana subduction history. *Geochemistry, Geophysics,*
907 *Geosystems*, 9(7).
- 908 DeMets, C., Gordon, R. G., Argus, D. F., & Stein, S. (1994). Effect of recent re-
909 visions to the geomagnetic reversal time scale on estimates of current plate
910 motions. *Geophysical research letters*, 21(20), 2191–2194.
- 911 Dreger, D. S. (2003). TDMT_INV: Time domain seismic moment tensor inversion.
912 In *International geophysics* (Vol. 81, p. 1627). Elsevier.
- 913 Eberhart-Phillips, D., & Bannister, S. (2010). 3-D imaging of Marlborough, New
914 Zealand, subducted plate and strike-slip fault systems. *Geophysical Journal In-*
915 *ternational*, 182(1), 73–96.
- 916 Eberhart-Phillips, D., & Bannister, S. (2015). 3-D imaging of the northern Hiku-
917 rangi subduction zone, New Zealand: variations in subducted sediment, slab
918 fluids and slow slip. *Geophysical Journal International*, 201(2), 838–855.
- 919 Eberhart-Phillips, D., Bannister, S., & Reyners, M. (2017). Deciphering the 3-D
920 distribution of fluid along the shallow Hikurangi subduction zone using P-and
921 S-wave attenuation. *Geophysical Journal International*, 211(2), 1032–1045.
- 922 Eberhart-Phillips, D., Bannister, S., & Reyners, M. (2020). Attenuation in the man-
923 tle wedge beneath super-volcanoes of the Taupō Volcanic Zone, New Zealand.
924 *Geophysical Journal International*, 220(1), 703–723.
- 925 Eberhart-Phillips, D., Bannister, S., Reyners, M., & Henrys, S. (2020). *New*
926 *Zealand Wide model 2.2 seismic velocity and Qs and Qp models for New*
927 *Zealand [dataset]*. Retrieved from zenodo.org/record/3779523 doi:
928 10.5281/zenodo.3779523
- 929 Eberhart-Phillips, D., & Fry, B. (2017). A new scheme for joint surface wave and
930 earthquake travel-time inversion and resulting 3-D velocity model for the west-
931 ern North Island, New Zealand. *Physics of the Earth and Planetary Interiors*,
932 269, 98–111.

- 933 Eberhart-Phillips, D., & Fry, B. (2018). Joint local earthquake and teleseismic in-
934 version for 3-D velocity and Q in New Zealand. *Physics of the Earth and Plan-*
935 *etary Interiors*, 283, 48–66.
- 936 Eberhart-Phillips, D., Han, D.-H., & Zoback, M. D. (1989). Empirical relation-
937 ships among seismic velocity, effective pressure, porosity, and clay content in
938 sandstone. *Geophysics*, 54(1), 82–89.
- 939 Eberhart-Phillips, D., & Reyners, M. (1997). Continental subduction and three-
940 dimensional crustal structure: The northern South Island, New Zealand. *Jour-*
941 *nal of Geophysical Research: Solid Earth*, 102(B6), 11843–11861.
- 942 Eberhart-Phillips, D., & Reyners, M. (2012). Imaging the Hikurangi Plate inter-
943 face region, with improved local-earthquake tomography. *Geophysical Journal*
944 *International*, 190(2), 1221–1242.
- 945 Eberhart-Phillips, D., Reyners, M., & Bannister, S. (2015). A 3D QP attenuation
946 model for all of New Zealand. *Seismological Research Letters*, 86(6), 1655–
947 1663.
- 948 Eberhart-Phillips, D., Reyners, M., Chadwick, M., & Chiu, J.-M. (2005). Crustal
949 heterogeneity and subduction processes: 3-D Vp, Vp/Vs and Q in the south-
950 ern North Island, New Zealand. *Geophysical Journal International*, 162(1),
951 270–288.
- 952 Edbrooke, S., Heron, D., Forsyth, P., & Jongens, R. (2015). *Geological map of New*
953 *Zealand 1:1 000 000. GNS Science Geological Map 2*.
- 954 Ellis, S., Van Dissen, R., Eberhart-Phillips, D., Reyners, M., Dolan, J., & Nicol,
955 A. (2017). Detecting hazardous New Zealand faults at depth using seismic
956 velocity gradients. *Earth and Planetary Science Letters*, 463, 333–343.
- 957 Fagereng, r., & Ellis, S. (2009). On factors controlling the depth of interseismic cou-
958 pling on the Hikurangi subduction interface, New Zealand. *Earth and Plane-*
959 *tary Science Letters*, 278(1-2), 120–130.
- 960 Fichtner, A., Bunge, H.-P., & Igel, H. (2006a). The adjoint method in seismology: I.
961 Theory. *Physics of the Earth and Planetary Interiors*, 157(1-2), 86–104.
- 962 Fichtner, A., Bunge, H.-P., & Igel, H. (2006b). The adjoint method in seismology—:
963 II. Applications: traveltimes and sensitivity functionals. *Physics of the Earth*
964 *and Planetary Interiors*, 157(1-2), 105–123.
- 965 Fichtner, A., Kennett, B. L., Igel, H., & Bunge, H.-P. (2009). Full seismic wave-
966 form tomography for upper-mantle structure in the Australasian region using
967 adjoint methods. *Geophysical Journal International*, 179(3), 1703–1725.
- 968 Fichtner, A., Kennett, B. L., Igel, H., & Bunge, H.-P. (2010). Full waveform to-
969 mography for radially anisotropic structure: new insights into present and past
970 states of the Australasian upper mantle. *Earth and Planetary Science Letters*,
971 290(3-4), 270–280.
- 972 Fichtner, A., & Trampert, J. (2011a). Hessian kernels of seismic data function-
973 als based upon adjoint techniques. *Geophysical Journal International*, 185(2),
974 775–798.
- 975 Fichtner, A., & Trampert, J. (2011b). Resolution analysis in full waveform inversion.
976 *Geophysical Journal International*, 187(3), 1604–1624.
- 977 Francis, D., Bennett, D., & Courteney, S. (2004). Advances in understanding of
978 onshore East Coast Basin structure, stratigraphic thickness and hydrocarbon
979 generation. In *New zealand petroleum conference proceedings* (pp. 1–20).
- 980 Graves, R., Jordan, T. H., Callaghan, S., Deelman, E., Field, E., Juve, G., ... oth-
981 ers (2011). CyberShake: A physics-based seismic hazard model for southern
982 California. *Pure and Applied Geophysics*, 168(3), 367–381.
- 983 Hamling, I. J., Hreinsdóttir, S., Clark, K., Elliott, J., Liang, C., Fielding, E., ...
984 others (2017). Complex multifault rupture during the 2016 Mw 7.8 Kaikōura
985 earthquake, New Zealand. *Science*, 356(6334), eaam7194.
- 986 Heise, W., Caldwell, T. G., Bibby, H. M., & Bennie, S. L. (2010). Three-dimensional
987 electrical resistivity image of magma beneath an active continental rift, Taupo

- Volcanic Zone, New Zealand. *Geophysical Research Letters*, 37(10).

Henrys, S., Eberhart-Phillips, D., Bassett, D., Sutherland, R., Okaya, D., Savage, M., ... others (2020). Upper plate heterogeneity along the southern Hikurangi Margin, New Zealand. *Geophysical Research Letters*, 47(4), e2019GL085511.

Henrys, S., Reyners, M., Pecher, I., Bannister, S., Nishimura, Y., & Maslen, G. (2006). Kinking of the subducting slab by escalator normal faulting beneath the North Island of New Zealand. *Geology*, 34(9), 777–780.

Henrys, S., Wech, A., Sutherland, R., Stern, T., Savage, M., Sato, H., ... others (2013). SAHKE geophysical transect reveals crustal and subduction zone structure at the southern Hikurangi margin, New Zealand. *Geochemistry, Geophysics, Geosystems*, 14(7), 2063–2083.

Holden, C., Kaneko, Y., D'Anastasio, E., Benites, R., Fry, B., & Hamling, I. (2017). The 2016 Kaikōura earthquake revealed by kinematic source inversion and seismic wavefield simulations: Slow rupture propagation on a geometrically complex crustal fault network. *Geophysical Research Letters*, 44(22), 11–320.

Holdgate, G., & Grapes, R. (2015). Wairau basin and fault connections across Cook strait, New Zealand: Seismic and geological evidence. *Australian Journal of Earth Sciences*, 62(1), 95–121.

Hung, S.-H., Dahlen, F., & Nolet, G. (2001). Wavefront healing: a banana–doughnut perspective. *Geophysical Journal International*, 146(2), 289–312.

Husen, S., Smith, R. B., & Waite, G. P. (2004). Evidence for gas and magmatic sources beneath the Yellowstone volcanic field from seismic tomographic imaging. *Journal of Volcanology and Geothermal Research*, 131(3-4), 397–410.

Illsley-Kemp, F., Barker, S., Wilson, C. J., Chamberlain, C. J., Hreinsdóttir, S., Ellis, S., ... Wadsworth, F. B. (2021). Volcanic unrest at Taupoācr volcano in 2019: Causes, mechanisms and implications. *Geochemistry, Geophysics, Geosystems*, e2021GC009803.

Ito, H., DeVilbiss, J., & Nur, A. (1979). Compressional and shear waves in saturated rock during water-steam transition. *Journal of Geophysical Research: Solid Earth*, 84(B9), 4731–4735.

Kaneko, Y., & Chow, B. (2017). *Broadband East Coast Network (BEACON)*. International Federation of Digital Seismograph Networks. Retrieved from http://www.fdsn.org/networks/detail/2P_2017/ doi: 10.7914/SN/2P_2017

Kaneko, Y., Ito, Y., Chow, B., Wallace, L., Tape, C., Grapenthin, R., ... Hino, R. (2019). Ultra-long Duration of Seismic Ground Motion Arising From a Thick, Low-Velocity Sedimentary Wedge. *Journal of Geophysical Research: Solid Earth*, 124(10), 10347–10359.

Kaneko, Y., Wallace, L., Hamling, I. J., & Gerstenberger, M. C. (2018). Simple physical model for the probability of a subduction-zone earthquake following slow slip events and earthquakes: Application to the Hikurangi megathrust, New Zealand. *Geophysical Research Letters*, 45(9), 3932–3941.

King, P. R., & Thrasher, G. P. (1996). *Cretaceous-Cenozoic geology and petroleum systems of the Taranaki Basin, New Zealand* (Vol. 2). Institute of Geological & Nuclear Sciences.

Komatitsch, D., Ritsema, J., & Tromp, J. (2002). The spectral-element method, Beowulf computing, and global seismology. *Science*, 298, 1737–1742.

Komatitsch, D., & Tromp, J. (2002a). Spectral-element simulations of global seismic wave propagation—II. Three-dimensional models, oceans, rotation and self-gravitation. *Geophysical Journal International*, 150(1), 303–318.

Komatitsch, D., & Tromp, J. (2002b). Spectral-element simulations of global seismic wave propagation—I. Validation. *Geophysical Journal International*, 149(2), 390–412.

Krischer, L., Fichtner, A., Boehm, C., & Igel, H. (2018). Automated large-scale full seismic waveform inversion for North America and the North Atlantic. *Journal of Geophysical Research: Solid Earth*, 123(7), 5902–5928.

- 1043 Krischer, L., Fichtner, A., Zukauskaite, S., & Igel, H. (2015). Large-scale seismic in-
1044 version framework. *Seismological Research Letters*, *86*(4), 1198–1207.
- 1045 Lanza, F., Chamberlain, C., Jacobs, K., Warren-Smith, E., Godfrey, H., Kortink,
1046 M., ... others (2019). Crustal fault connectivity of the Mw 7.8 2016 Kaikōura
1047 earthquake constrained by aftershock relocations. *Geophysical Research Let-
1048 ters*, *46*(12), 6487–6496.
- 1049 Lewis, K., & Pettinga, J. (1993). The emerging, imbricate frontal wedge of the Hiku-
1050 rangi margin. *Sedimentary Basins of the World*, *2*, 225–250.
- 1051 Litchfield, N., Ellis, S., Berryman, K., & Nicol, A. (2007). Insights into subduction-
1052 related uplift along the Hikurangi Margin, New Zealand, using numerical
1053 modeling. *Journal of Geophysical Research: Earth Surface*, *112*(F2).
- 1054 Litchfield, N., Van Dissen, R., Sutherland, R., Barnes, P., Cox, S., Norris, R., ...
1055 others (2014). A model of active faulting in New Zealand. *New Zealand
1056 Journal of Geology and Geophysics*, *57*(1), 32–56.
- 1057 Little, T. A., & Roberts, A. P. (1997). Distribution and mechanism of Neogene
1058 to present-day vertical axis rotations, Pacific-Australian plate boundary zone,
1059 South Island, New Zealand. *Journal of Geophysical Research: Solid Earth*,
1060 *102*(B9), 20447–20468.
- 1061 Lomax, A., Virieux, J., Volant, P., & Berge-Thierry, C. (2000). Probabilistic earth-
1062 quake location in 3D and layered models. In *Advances in seismic event location*
1063 (pp. 101–134). Springer.
- 1064 Maggi, A., Tape, C., Chen, M., Chao, D., & Tromp, J. (2009). An automated time-
1065 window selection algorithm for seismic tomography. *Geophysical Journal Inter-
1066 national*, *178*(1), 257–281.
- 1067 Marquering, H., Dahlen, F., & Nolet, G. (1999). Three-dimensional sensitivity ker-
1068 nels for finite-frequency traveltimes: the banana-doughnut paradox. *Geophysi-
1069 cal Journal International*, *137*(3), 805–815.
- 1070 Miyoshi, T., Obayashi, M., Peter, D., Tono, Y., & Tsuboi, S. (2017). Adjoint tomog-
1071 raphy of the crust and upper mantle structure beneath the Kanto region using
1072 broadband seismograms. *Progress in Earth and Planetary Science*, *4*(1), 1–20.
- 1073 Mochizuki, K., Sutherland, R., Henrys, S., Bassett, D., Van Avendonk, H., Arai, R.,
1074 ... others (2019). Recycling of depleted continental mantle by subduction and
1075 plumes at the Hikurangi Plateau large igneous province, southwestern Pacific
1076 Ocean. *Geology*, *47*(8), 795–798.
- 1077 Modrak, R., Borisov, D., Lefebvre, M., & Tromp, J. (2018). SeisFlows — Flexible
1078 waveform inversion software. *Computers & Geosciences*, *115*, 88–95.
- 1079 Modrak, R., & Tromp, J. (2016). Seismic waveform inversion best practices: re-
1080 gional, global and exploration test cases. *Geophysical Journal International*,
1081 *206*(3), 1864–1889.
- 1082 Montelli, R., Nolet, G., Dahlen, F., Masters, G., Engdahl, E. R., & Hung, S.-H.
1083 (2004). Finite-frequency tomography reveals a variety of plumes in the mantle.
1084 *Science*, *303*(5656), 338–343.
- 1085 Mortimer, N. (2004). New Zealand's geological foundations. *Gondwana research*,
1086 *7*(1), 261–272.
- 1087 Mortimer, N., & Parkinson, D. (1996). Hikurangi Plateau: A Cretaceous large
1088 igneous province in the southwest Pacific Ocean. *Journal of Geophysical Re-
1089 search: Solid Earth*, *101*(B1), 687–696.
- 1090 Nazarian, S., & Stokoe, K. H. (1984). Nondestructive testing of pavements using
1091 surface waves. *Transportation Research Record*, *993*, 67–79.
- 1092 Nicol, A., & Beavan, J. (2003). Shortening of an overriding plate and its implica-
1093 tions for slip on a subduction thrust, central Hikurangi Margin, New Zealand.
1094 *Tectonics*, *22*(6).
- 1095 Nicol, A., Mazengarb, C., Chanier, F., Rait, G., Uruski, C., & Wallace, L. (2007).
1096 Tectonic evolution of the active Hikurangi subduction margin, New Zealand,
1097 since the Oligocene. *Tectonics*, *26*(4).

- 1098 Nocedal, J., & Wright, S. (2006). *Numerical optimization*. Springer Science & Busi-
1099 ness Media.
- 1100 Nolet, G. (2008). A breviary of seismic tomography. *A Breviary of Seismic Tomog-
1101 raphy*.
- 1102 Pondard, N., & Barnes, P. M. (2010). Structure and paleoearthquake records of
1103 active submarine faults, Cook Strait, New Zealand: Implications for fault in-
1104 teractions, stress loading, and seismic hazard. *Journal of Geophysical Research: Solid
1105 Earth*, 115(B12).
- 1106 Reyners, M., Eberhart-Phillips, D., & Bannister, S. (2011). Tracking repeated sub-
1107 duction of the Hikurangi Plateau beneath New Zealand. *Earth and Planetary
1108 Science Letters*, 311(1-2), 165–171.
- 1109 Reyners, M., Eberhart-Phillips, D., & Bannister, S. (2017). Subducting an old
1110 subduction zone sideways provides insights into what controls plate coupling.
Earth and Planetary Science Letters, 466, 53–61.
- 1111 Reyners, M., Eberhart-Phillips, D., Stuart, G., & Nishimura, Y. (2006). Imaging
1112 subduction from the trench to 300 km depth beneath the central North Island,
1113 New Zealand, with Vp and Vp/Vs. *Geophysical Journal International*, 165(2),
1114 565–583.
- 1115 Ristau, J. (2008). Implementation of routine regional moment tensor analysis in
1116 New Zealand. *Seismol. Res. Lett.*, 79(3), 400–415. doi: 10.1785/gssrl.79.3.400
- 1117 Ruan, Y., Lei, W., Modrak, R., Örsvuran, R., Bozdağ, E., & Tromp, J. (2019).
1118 Balancing unevenly distributed data in seismic tomography: a global adjoint
1119 tomography example. *Geophysical Journal International*, 219(2), 1225–1236.
- 1120 Sherburn, S., & White, R. S. (2006). Tectonics of the Taranaki region, New Zealand:
1121 earthquake focal mechanisms and stress axes. *New Zealand Journal of Geology
1122 and Geophysics*, 49(2), 269–279.
- 1123 Sherburn, S., White, R. S., & Chadwick, M. (2006). Three-dimensional tomographic
1124 imaging of the Taranaki volcanoes, New Zealand. *Geophysical Journal Interna-
1125 tional*, 166(2), 957–969.
- 1126 Stagpoole, V., Miller, C., Caratori Tontini, F., Brakenrig, T., & Macdonald, N.
1127 (2020). A two million-year history of rifting and caldera volcanism imprinted
1128 in new gravity anomaly compilation of the Taupō Volcanic Zone, New Zealand.
New Zealand Journal of Geology and Geophysics, 1–14.
- 1129 Stern, T. (1985). A back-arc basin formed within continental lithosphere: the Cen-
1130 tral Volcanic Region of New Zealand. *Tectonophysics*, 112(1-4), 385–409.
- 1131 Sutherland, R., Eberhart-Phillips, D., Harris, R., Stern, T., Beavan, J., Ellis, S., ...
1132 others (2007). Do great earthquakes occur on the Alpine fault in central South
1133 Island, New Zealand? *Geophysical Monograph - American Geophysical Union*,
1134 175, 237.
- 1135 Tao, K., Grand, S. P., & Niu, F. (2018). Seismic structure of the upper mantle be-
1136 neath eastern Asia from full waveform seismic tomography. *Geochemistry, Geo-
1137 physics, Geosystems*, 19(8), 2732–2763.
- 1138 Tape, C., Liu, Q., Maggi, A., & Tromp, J. (2010). Seismic tomography of the south-
1139 ern California crust based on spectral-element and adjoint methods. *Geophys-
1140 ical Journal International*, 180(1), 433–462.
- 1141 Tape, C., Liu, Q., & Tromp, J. (2007). Finite-frequency tomography using ad-
1142 joint methods—Methodology and examples using membrane surface waves.
Geophysical Journal International, 168(3), 1105–1129.
- 1143 Tarantola, A. (1984). Inversion of seismic reflection data in the acoustic approxima-
1144 tion. *Geophysics*, 49(8), 1259–1266.
- 1145 Tarantola, A. (2005). *Inverse problem theory and methods for model parameter esti-
1146 mation* (Vol. 89). Siam.
- 1147 Taylor, B. (2006). The single largest oceanic plateau: Ontong Java-Manihiki–
1148 Hikurangi. *Earth and Planetary Science Letters*, 241(3-4), 372–380.
- 1149

- 1152 Thrastarson, S., van Herwaarden, D.-P., & Fichtner, A. (2021). Inversionson: Fully
1153 Automated Seismic Waveform Inversions.
- 1154 Townend, J., Sherburn, S., Arnold, R., Boese, C., & Woods, L. (2012). Three-
1155 dimensional variations in present-day tectonic stress along the Australia-
1156 Pacific plate boundary in New Zealand. *Earth and Planetary Science Letters*,
1157 353, 47–59.
- 1158 Tromp, J., Tape, C., & Liu, Q. (2005). Seismic tomography, adjoint methods, time
1159 reversal and banana-doughnut kernels. *Geophysical Journal International*,
1160 160(1), 195–216.
- 1161 Ukawa, M., & Fukao, Y. (1981). Poisson's ratios of the upper and lower crust and
1162 the sub-Moho mantle beneath central Honshu, Japan. *Tectonophysics*, 77(3-4),
1163 233–256.
- 1164 Uruski, C. (1992). Sedimentary Basins and structure of Cook Strait. *Institute of Ge-
1165 ological and Nuclear Sciences Science Report 92/03*.
- 1166 Villamor, P., & Berryman, K. (2006). Evolution of the southern termination of the
1167 Taupō Rift, New Zealand. *New Zealand Journal of Geology and Geophysics*,
1168 49(1), 23–37.
- 1169 Villamor, P., Berryman, K., Ellis, S., Schreurs, G., Wallace, L., Leonard, G., ...
1170 Ries, W. (2017). Rapid evolution of subduction-related continental intraarc
1171 rifts: The Taupo Rift, New Zealand. *Tectonics*, 36(10), 2250–2272.
- 1172 Wallace, L. (2020). Slow slip events in New Zealand. *Annual Review of Earth and
1173 Planetary Sciences*, 48, 175–203.
- 1174 Wallace, L., Barnes, P., Beavan, J., Van Dissen, R., Litchfield, N., Mountjoy, J., ...
1175 Pondard, N. (2012). The kinematics of a transition from subduction to strike-
1176 slip: An example from the central New Zealand plate boundary. *Journal of
1177 Geophysical Research: Solid Earth*, 117(B2).
- 1178 Wallace, L., & Beavan, J. (2006). A large slow slip event on the central Hiku-
1179 rangi subduction interface beneath the Manawatu region, North Island, New
1180 Zealand. *Geophysical Research Letters*, 33(11).
- 1181 Wallace, L., Beavan, J., Bannister, S., & Williams, C. (2012). Simultaneous long-
1182 term and short-term slow slip events at the Hikurangi subduction margin,
1183 New Zealand: Implications for processes that control slow slip event occur-
1184 rence, duration, and migration. *Journal of Geophysical Research: Solid Earth*,
1185 117(B11).
- 1186 Wallace, L., Beavan, J., McCaffrey, R., Berryman, K., & Denys, P. (2007). Bal-
1187 ancing the plate motion budget in the South Island, New Zealand using GPS,
1188 geological and seismological data. *Geophysical Journal International*, 168(1),
1189 332–352.
- 1190 Wallace, L., Beavan, J., McCaffrey, R., & Darby, D. (2004). Subduction zone cou-
1191 pling and tectonic block rotations in the North Island, New Zealand. *Journal
1192 of Geophysical Research: Solid Earth*, 109(B12).
- 1193 Wallace, L., Cochran, U. A., Power, W. L., & Clark, K. J. (2014). Earthquake and
1194 tsunami potential of the Hikurangi subduction thrust, New Zealand: Insights
1195 from paleoseismology, GPS, and tsunami modeling. *Oceanography*, 27(2),
1196 104–117.
- 1197 Wallace, L., Reyners, M., Cochran, U., Bannister, S., Barnes, P., Berryman, K.,
1198 ... Power, W. (2009). Characterizing the seismogenic zone of a major plate
1199 boundary subduction thrust: Hikurangi Margin, New Zealand. *Geochemistry,
1200 Geophysics, Geosystems*, 10(10). doi: 10.1029/2009GC002610
- 1201 Webb, S. C. (1998). Broadband seismology and noise under the ocean. *Reviews of
1202 Geophysics*, 36(1), 105–142.
- 1203 Williams, C., Eberhart-Phillips, D., Bannister, S., Barker, D., Henrys, S., Reyners,
1204 M., & Sutherland, R. (2013). Revised interface geometry for the Hikurangi
1205 subduction zone, New Zealand. *Seismological Research Letters*, 84(6), 1066–
1206 1073.

manuscript submitted to *JGR: Solid Earth*

- 1207 Williams, C., & Wallace, L. (2018). The impact of realistic elastic properties on in-
1208 verersions of shallow subduction interface slow slip events using seafloor geodetic
1209 data. *Geophysical Research Letters*, 45(15), 7462–7470.
- 1210 Wilson, C., Gravley, D., Leonard, G., & Rowland, J. (2009). Volcanism in the cen-
1211 tral Taupo Volcanic Zone, New Zealand: tempo, styles and controls. *Studies in*
1212 *Volcanology: the Legacy of George Walker. Special Publications of IAVCEI*, 2,
1213 225–247.
- 1214 Wilson, C., Houghton, B., McWilliams, M., Lanphere, M., Weaver, S., & Briggs,
1215 R. (1995). Volcanic and structural evolution of Taupo Volcanic Zone, New
1216 Zealand: a review. *Journal of Volcanology and Geothermal Research*, 68(1-3),
1217 1–28.
- 1218 Zhao, L., Jordan, T. H., & Chapman, C. H. (2000). Three-dimensional Fréchet
1219 differential kernels for seismic delay times. *Geophysical Journal International*,
1220 141(3), 558–576.
- 1221 Zhu, H., Bozdağ, E., & Tromp, J. (2015). Seismic structure of the European up-
1222 per mantle based on adjoint tomography. *Geophysical Journal International*,
1223 201(1), 18–52.